Title: A basally active cGAS-STING pathway limits SARS-CoV-2 replication in a subset of ACE2 positive airway cell models

Maritza Puray-Chavez[1], Kyle M. LaPak[2], Ria Jasuja[2], Jiehong Pan[3], Jian Xu[3], Jenna E. Eschbach[1], Shawn Mohammed[1], Dana Q. Lawson[1], Qibo Wang[1], Steven L. Brody[3], Michael B. Major[2,4], Dennis Goldfarb[2,5], Sebla B. Kutluay[1,*]

[1]Department of Molecular Microbiology, Washington University in St. Louis, St. Louis, MO, USA

[2]Department of Cell Biology and Physiology, Washington University in St. Louis, St. Louis, MO, USA

[3]Division of Pulmonary and Critical Care Medicine, Department of Medicine, Washington University in St. Louis, School of Medicine, St. Louis, MO, USA

[4]Department of Otolaryngology, Washington University in St. Louis, St. Louis, MO, USA

[5]Institute for Informatics, Data Science & Biostatistics, Washington University in St. Louis, St. Louis, MO, USA.

Running title: Basally active cGAS-STING limits SARS-CoV-2 infection

*Correspondence: kutluay@wustl.edu (S.B.K.)

ABSTRACT

Host factors that define the cellular tropism of SARS-CoV-2 beyond the cognate ACE2 receptor are poorly defined. From a screen of human airway derived cell lines that express varying levels of ACE2/TMPRSS2, we found a subset that express comparably high endogenous levels of ACE2 but surprisingly did not support SARS-CoV-2 replication. Here we report that this resistance is mediated by a basally active cGAS-STING pathway culminating in interferon (IFN)-mediated restriction of SARS-CoV-2 replication at a post-entry step. Pharmacological inhibition of JAK1/2, depletion of the IFN-α receptor and cGAS-STING pathway effectors substantially increased SARS-CoV-2 replication in these cell models. While depletion of cGAS or STING was sufficient to reduce the preexisting levels of IFN-stimulated genes (ISGs), SARS-CoV-2 infection in STING knockout cells independently induced ISG expression. Remarkably, SARS-CoV-2-induced ISG expression in STING knockout cell as well as in primary human airway cultures was limited to uninfected bystander cells, demonstrating efficient antagonism of the type I/III IFN-pathway, but not viral sensing or IFN production, in productively infected cells. Of note, SARS-CoV-2-infected primary human airway cells also displayed markedly lower levels of STING expression, raising the possibility that SARS-CoV-2 can target STING expression or preferentially infect cells that express low levels of STING. Finally, ectopic ACE2 overexpression overcame the IFN-mediated blocks, suggesting the ability of SARS-CoV-2 to overcome these possibly saturable blocks to infection. Our study highlights that in addition to viral receptors, basal activation of the cGAS-STING pathway and innate immune defenses may contribute to defining SARS-CoV-2 cellular tropism.

44 **INTRODUCTION**

45 Severe acute respiratory syndrome coronavirus 2 (SARS-CoV-2) is continuing to cause significant
46 respiratory disease and mortality in vulnerable populations. The emergence of highly
47 transmissible viral variants resistant to vaccines and existing immunity is an ongoing concern [1-6].
48 The innate immune response mediated by type I, type II and type III interferons (IFNs) constitutes
49 a potent block to SARS-CoV-2 replication [7-12]. It remains unknown if IFN-mediated antiviral
50 responses can modulate the cellular tropism of SARS-CoV-2 independently of the cognate host
51 cell SARS-CoV-2 receptor, ACE2. Given the multiple ways in which SARS-CoV-2 can antagonize
52 IFN production and signaling [13-22], a comprehensive understanding of the interplay between these
53 mechanisms may inform the observed multi-organ involvement, reveal new facets of emerging
54 SARS-CoV-2 variants and ultimately identify new opportunities for therapeutic intervention.

55 SARS-CoV-2 homotrimeric spike (S) glycoprotein binding to the host cell angiotensin converting
56 enzyme 2 (ACE2) receptor mediates viral entry [23-26]. Endogenous ACE2 expression is surprisingly
57 low in the respiratory tract [27,28] compared with higher levels in other tissues of the gastrointestinal
58 tract, kidney and myocardium [29-35]. Although ectopic expression of ACE2 is sufficient for viral entry
59 in several cell culture and animal models, additional factors may contribute to defining the cellular
60 tropism of SARS-CoV-2 [23-26,36-39]. Growing evidence suggests that viral attachment factors can
61 facilitate ACE2-dependent [40-45] and even enable ACE2-independent entry [46-49]. Together, these
62 alternative receptors and attachment factors may compensate for the low levels of ACE2
63 expression in various organs, including the distal respiratory system.

64 In addition to the identity and expression of entry factors and receptors, SARS-CoV-2 cellular
65 tropism may be determined by cell intrinsic and innate immune defenses given the well-
66 established antiviral effects of IFN [8-12,22,50] that act through the effector functions of one or more
67 ISGs [51-56]. In agreement, a preactivated antiviral innate immunity in the upper airways of young

68 children has been proposed to limit SARS-CoV-2 replication [57]. In addition, at a basal level,
69 microbiota can also promote antiviral innate immunity through type I/III IFNs [58-62]. For example,
70 beneficial lactic acid gut bacteria as well as extracellular vesicles from the fungal commensal
71 *Candida albicans* can activate type I IFN production through cytosolic sensors cGAS/STING and
72 MAVS [60,63]. Recent evidence points to a similar role for cGAS/STING-dependent innate immune
73 activation upon sensing of endogenous retroviruses in skin keratinocytes [62]. Interestingly,
74 disruptions in microbiota homeostasis in the respiratory and gastrointestinal tracts, the primary
75 targets of SARS-CoV-2 [64-67], have been observed in hospitalized COVID-19 patients [68-72].

76 Despite the known antiviral effects of IFN pretreatment on SARS-CoV-2 replication [8-12,22,50],
77 SARS-CoV-2 itself can induce the production of type I IFNs, albeit this response appears to be
78 delayed compared to other viruses whereas other proinflammatory cytokines remain elevated
79 [12,14,73-75]. This delay can partly be ascribed to the actions of numerous virally encoded proteins
80 that can antagonize IFN synthesis or subsequent IFN signaling pathways [13-22]. We and others
81 have shown that the RIG-I-like receptors (RLRs), RIG-I and MDA5, mediate the detection of
82 SARS-CoV-2 replication in infected cells [76-82] leading to the induction of observed IFN responses.
83 Taken together, it is plausible that cellular tropism of SARS-CoV-2 is shaped by ACE2 expression
84 levels, innate immune activation state of the target cells and distinct viral proteins that antagonize
85 the host cell antiviral responses.

86 We previously screened 10 human lung and upper airway cell lines expressing variable levels of
87 endogenous ACE2/TMPRSS2. Unexpectedly, we found that several cell lines that expressed
88 comparably higher levels of ACE2 (from here on referred to as ACE2(high)) were not permissive
89 to infection [76]. In this study, we sought to understand the molecular basis of this resistance.
90 Analysis of the transcriptomic signatures of our cell line panel revealed markedly higher levels of
91 ISGs and IFN pathway mediators in the ACE2(high) cells. Pharmacological inhibition of the IFN
92 pathway or its disruption by RNAi/CRISPR enhanced SARS-CoV-2 replication in a subset of these

93 cell models. A targeted genetic screen in a representative ACE2(high) cell line revealed that
94 constitutive activation of the cGAS-STING pathway underlies the observed IFN pathway activity.
95 Genetic disruption of the cGAS-STING pathway substantially decreased baseline ISG expression
96 and enhanced virus replication in three separate ACE2(high) cell lines. In addition to the ablation
97 of the cGAS/STING pathway, ACE2 overexpression also overcame the IFN-mediated blocks to
98 SARS-CoV-2 replication, demonstrating the ability of SARS-CoV-2 to overcome these possibly
99 saturable blocks to infection. SARS-CoV-2 replication in STING$^{-/-}$ cells and in primary human
100 airway cultures triggered type I IFN pathway activation. However, in these settings, ISG
101 expression was primarily limited to uninfected bystander cells, suggesting efficient antagonism
102 of the IFN signaling pathway, but not viral sensing or IFN synthesis, in infected cells. Interestingly,
103 in primary human airway cultures, SARS-CoV-2-infected cells also displayed markedly lower
104 levels of STING expression, raising the possibility that SARS-CoV-2 can target STING expression
105 or preferentially infect cells that express low levels of STING.

106 Taken together, our findings demonstrate that cGAS-STING-dependent activation of IFN-
107 mediated innate immunity underlies the inability of a subset of ACE2 positive airway cell lines to
108 support SARS-CoV-2 replication. Our study highlights that in addition to ACE2 levels, basal
109 activation of the cGAS-STING and subsequent IFN pathways contribute to defining the SARS-
110 CoV-2 cellular tropism *in vitro*.

111 **RESULTS**

112 ***SARS-CoV-2 replication is blocked at a post-entry stage in a subset of airway-derived cell***
113 ***lines that endogenously express ACE2.***

114 We previously screened 10 human lung and upper airway cell lines expressing variable levels of
115 endogenous ACE2/TMPRSS2 for their ability to support SARS-CoV-2 replication [76].
116 Unexpectedly, we found four cell models—SCC25, H596, OE21 and Detroit 562—that express

117 high levels of ACE2 mRNA (**Fig. S1A**) and protein [76] but were resistant to SARS-CoV-2 replication
118 [76]. Of note, these initial screens were conducted with a SARS-CoV-2 stock carrying the S E484D
119 substitution, which arises consistently during cell culture adaptation and allows virus replication
120 in an ACE2-independent manner [76,83]. Given this possible complication, we first validated the
121 ability of virus stocks verified to bear wild type (WT) S to infect these ACE2 expressing cells.
122 SARS-CoV-2 WT S productively infected PC-9, KYSE-30 and H1299 cells that express
123 comparably lower levels of ACE2 (**Fig. S1A**) in addition to the control Calu-3 and HCC827 cells,
124 as evident from the substantial increase in the amount of cell-associated viral RNA (**Fig. 1A**), viral
125 N antigen (**Fig. S1B**) and infectious virion release in cell culture supernatants (**Fig. 1B**) following
126 virus inoculation. CRISPR-mediated knockout of ACE2 significantly decreased cell-associated
127 SARS-CoV-2 RNA levels in these cells (**Fig. 1C**), validating the ACE2-dependence of virus
128 replication. In agreement with our prior findings [76], other cell lines including SCC25, H596, OE21
129 and Detroit 562 that expressed higher levels of ACE2 were largely resistant to SARS-CoV-2
130 replication (**Fig. 1A-C, S1B**). Importantly, we found that ACE2 knockout led to a significant
131 reduction in incoming cell-associated SARS-CoV-2 RNA in the ACE2(high) cell lines (**Fig. 1D, E**),
132 suggesting a post-entry block to virus replication and spread. These results demonstrate that
133 ACE2 expression and viral entry is not sufficient to allow productive SARS-CoV-2 replication in
134 the ACE2(high) SCC25, H596, OE21, and Detroit 562 cell lines.

135 ***ACE2(high) airway-derived cell lines express high baseline levels of IFN pathway genes***

136 A common block to SARS-CoV-2 replication is mediated by type I and type III IFNs [7-9], as also
137 exemplified by potent inhibition of SARS-CoV-2 replication by IFN-α pretreatment of Calu-3 cells
138 (**Fig. S2A**). Seeking to understand if IFN pathway activity contributed to SARS-CoV-2 resistance
139 in ACE2(high) SCC25, H596, OE21, and Detroit 562 cells, we first evaluated the expression of
140 IFN pathway response genes by RNA-seq. Strikingly, transcriptomic signatures of the cell line
141 panel revealed substantially higher basal expression levels of numerous ISGs as well as IFN

142 pathway components in the ACE2(high) cells compared to those that express low to no ACE2
143 (**Fig. 2A**). RT-qPCR and immunoblotting confirmed this observation and showed markedly high
144 baseline expression of several ISGs and IFN-pathway mediators (i.e. *MX1*, *IFIT1*, *STAT1*,
145 *pSTAT1*, *IRF7* and *IRF9*) in SCC25, H596, OE21 and Detroit 562 cells (**Fig. 2B-F, S2B, S2C**).
146 Further investigation of the RNA-seq data revealed elevated levels of type I and type III IFNs in
147 the ACE2(high) SCC25, H596, OE21 but not Detroit 562 cells (**Fig. S2D**). In addition to the basally
148 high ISG levels, SCC25, H596, OE21 and Detroit 562 cells responded to SARS-CoV-2 inoculation
149 by further upregulating ISG expression (**Fig. 2G, 2H, S2D-G**). Collectively, these findings suggest
150 that the basally high levels of ISG expression, coupled with further elevation of ISG expression
151 upon SARS-CoV-2 inoculation, may underlie the post-entry block to infection in the ACE2(high)
152 SCC25, H596, OE21 and Detroit 562 cells.

153 ***Basally active type I/III IFN signaling pathway underlies the resistance of ACE2(high) cell***
154 ***lines to SARS-CoV-2 replication***

155 Canonically, binding of type I/III IFNs to cell surface receptors results in JAK1/TYK2 mediated
156 phosphorylation of STAT1 and STAT2, which subsequently form a complex with IRF9 and
157 translocate to the nucleus to activate the transcription of ISGs [84-87]. To evaluate whether the
158 constitutive activity of this pathway underlies the resistance of SCC25, H596, OE21 and Detroit
159 562 cells to SARS-CoV-2 infection, cells were pretreated with ruxolitinib, a JAK1/2 inhibitor, and
160 inoculated with SARS-CoV-2 in its presence. Ruxolitinib treatment decreased the baseline
161 expression of five canonical ISGs (*Ifit1*, *Mx1, Ifit2, Ish15* and *Irf9*) in SCC25 cells (**Fig. 3A, 3B,**
162 **S3A-D**). Subsets of these ISGs were also suppressed in the other ACE2(high) cell models (**Fig.**
163 **3A, 3B, S3A-D**). Ruxolitinib treatment resulted in an approximate 3-log increase in the amount of
164 cell-associated SARS-CoV-2 RNA in OE21 and SCC25, but not in Detroit 562 or H596 cells (**Fig.**
165 **3C**). Because of this, we decided to focus our studies on SCC25 cells with validation experiments

166 primarily in OE21 cells. In agreement with the ruxolitinib data, siRNA-mediated depletion of
167 downstream IFN pathway components STAT2, IRF9 (**Fig. S3E, S3F)** and CRISPR-mediated
168 knockout of IFNAR enhanced SARS-CoV-2 replication in SCC25 cells (**Fig. 3D-F**). In contrast,
169 siRNA knockdown of STAT1 (**Fig. S3G, S3H)** did not restore SARS-CoV-2 replication (**Fig. 3G**).
170 Together, these data suggest that the high baseline activity of the type I/III IFN signaling, possibly
171 independent of STAT1, underlies the inability of OE21 and SCC25 cells to support SARS-CoV-2
172 replication.

173 ***A basally active cGAS-STING pathway underlies the resistance of SCC25, OE21 and Det562***
174 ***cells to SARS-CoV-2 replication***

175 To identify the molecular basis of the basally high IFN pathway activity in the SCC25 cells, we
176 conducted an siRNA screen (2 siRNAs/target) targeting host cell factors involved in sensing of
177 virus replication intermediates including TLRs (e.g. TLR3, TLR7, TLR8 and TLR9), RLRs (e.g.
178 RIG-I, MDA5 and LGP2) as well as their downstream adaptor molecules (e.g. MyD88, TRIF and
179 MAVS), NOD-like receptor family members (i.e. NOD2, NLRP1, NLRP3 and NLRC5) and the
180 cytosolic DNA sensor STING. Remarkably, depletion of STING by two independent siRNAs
181 substantially increased (~2-3-logs) cell-associated viral RNA levels in SCC25 cells (**Fig. 4A**).
182 Although knockdown of other sensors and downstream adaptors by individual siRNAs increased
183 viral RNA levels up to 10-fold, effects were comparably modest and siRNA-specific (**Fig. 4A**).
184 Consistent with the screening results, CRISPR-mediated knockout of cGAS, STING as well as
185 downstream signaling molecules TBK1 and IRF3 significantly increased cell-associated viral RNA
186 (**Fig. 4B**) and antigen levels (**Fig. 4C**). Depletion of cGAS-STING pathway components or STING
187 knockout also enhanced SARS-CoV-2 replication in the ACE2(high) OE21 and Detroit 562, but
188 not in H596 cells (**Fig. S4A-C**). In addition, STING knockout did not enhance virus replication
189 further in the otherwise permissive cells (**Fig. S4B, S4C**). As expected, a greater number of
190 STING KO SCC25 cells were infected with a NeonGreen reporter SARS-CoV-2 (SARS-CoV-2

191 mNG) compared with the control SCC25 NT cells at 24 hpi (**Fig. 4D, S4D**). However, we noted
192 that virus spread was limited at later time points in infection (**Fig. 4D, S4D**). Ruxolitinib
193 pretreatment of STING KO cells allowed greater virus spread (**Fig. 4E**), suggesting the possibility
194 that SARS-CoV-2-induced type I/III IFN response contributes to the observed restriction of viral
195 spread. Collectively, these results suggest that the basally active cGAS-STING and downstream
196 type I/III IFN signaling pathways underlie the resistance to SARS-CoV-2 infection in several
197 ACE2(high) cell line models. While ablation of this pathway enhances SARS-CoV-2 replication
198 early, induction of the type I/III IFN responses at later time points post-infection limits spreading
199 infection.

200 ***SARS-CoV-2 antagonizes the IFN pathway activity in infected cells***

201 The limited virus spread in STING KO SCC25 cells prompted us to further investigate the interplay
202 between cGAS-STING-mediated activation of the IFN pathway and SARS-CoV-2 infection. First,
203 we found that CRISPR-mediated knockout of cGAS and STING substantially reduced the
204 baseline expression of ISGs including *Isg15, Ifit1, Ifit2, Ifit3, and Irf7* in uninfected cells (**Fig. 5A,**
205 **B**), strongly suggesting that the cGAS-STING pathway is indeed responsible for maintaining high
206 expression levels of ISGs in SCC25 cells. Notwithstanding, SARS-CoV-2 replication in cGAS and
207 STING KO SCC25 cells was still capable of inducing substantial increases in ISGs expression
208 (**Fig. 5C**), nearing levels observed in WT SCC25 cells (**Fig. 5D**). Most notably, in SARS-CoV-2-
209 infected STING KO cells, ISG induction, as exemplified by IFIT3, was largely limited to uninfected
210 bystander cells; cells infected with SARS-CoV-2 were largely devoid of IFIT3 (**Fig. 5E, S5A**).
211 Interestingly, the repressive effects of the type I/III IFN pathway were overcome by ACE2
212 overexpression in SCC25, OE21, H596 and Detroit 562 cells (**Fig. S5B**) and ruxolitinib treatment
213 did not further enhance virus replication (**Fig. S5C**). It has been reported that the VOCs are
214 generally less sensitive to the inhibitory effects of type I IFNs [88]. Ruxolitinib pretreatment
215 enhanced virus replication 2-3 logs in SCC25 cells for most of the VOCs with the exception of the

216 Delta and Kappa variant strains which responded to ruxolitinib treatment only modestly (**Fig.**
217 **S5D**). These findings collectively suggest that SARS-CoV-2 can efficiently antagonize IFN
218 signaling but not IFN production in infected cells and that IFN signaling in bystander cells limits
219 viral spread in settings where ACE2 is expressed at endogenous levels.

220 ***In primary airway cultures, SARS-CoV-2 induces ISG expression in bystander and***
221 ***antagonizes STING expression in infected cells***

222 To extend the findings from our cell line studies to a physiologically relevant model, we next
223 investigated the expression levels of a representative ISG (i.e. IFIT2) and STING in primary
224 human airway epithelial cells (hTECs) grown at the air-liquid interface. Of the two donors
225 analyzed, Donor 1 appeared to express higher baseline levels of IFIT2 in a subset of cells (**Fig.**
226 **6A**). SARS-CoV-2 infection resulted in a substantial increase in IFIT2 expression in both donors
227 (**Fig.6A**). Remarkably, as in the SCC25 cell model, IFIT2 expression was largely limited to
228 uninfected bystander cells (**Fig. 6A**, **S6A, S6B**). Both hTECs donors endogenously expressed
229 STING with Donor 2 donor expressing higher levels at baseline (**Fig. S6C**). Note that anti-STING
230 antibody specificity was further evaluated in SCC25 STING CRISPR KO cells (**Fig. S6D**). SARS-
231 CoV-2 infection resulted in a modest increase in STING expression; however, we found that
232 infected cells (as assessed by N antigen staining) were largely devoid of STING (**Fig. 6B, S6A,**
233 **S6B**). Analysis of publicly accessible single-cell data sets revealed STING and ISG expression in
234 healthy alveolar type-1 (AT1) human airway cells but not in alveolar type-2 (AT2) cells (**Fig. 7**),
235 which are the primary targets of SARS-CoV-2 [25,35,89]. Together, these findings raise the possibility
236 that SARS-CoV-2 can target STING expression or preferentially infect cells that express low
237 levels of STING. Nonetheless, basal expression levels of ISGs as well as their induction in
238 bystander cells appear to limit SARS-CoV-2 spread in these relevant models that express low
239 levels of ACE2.

240 **DISCUSSION**

241 Because ectopic expression of ACE2 allows efficient SARS-CoV-2 replication in numerous cell
242 lines and animal models [23-26,36-39], it is generally thought that ACE2 is the main factor that defines
243 the cellular tropism of SARS-CoV-2. Our findings challenge this notion and demonstrate that in
244 cells that express endogenous levels of ACE2, baseline activation of the type I/III IFN pathway
245 efficiently limits virus replication at a post-entry step. Interestingly, we found that ectopic
246 expression of ACE2 overcomes the ISG-mediated restriction to SARS-CoV-2 replication in these
247 cell models (**Fig. S5B, S5C**), suggesting the ability of SARS-CoV-2 to antagonize these blocks at
248 higher multiplicities of infection and possibly their saturable nature. In addition to providing novel
249 insight to molecular mechanisms that govern the cellular tropism of SARS-CoV-2, the
250 ACE2(high)/ISG(high) cells studied here can serve as unique models to study the molecular
251 details of innate host responses against SARS-CoV-2.

252 Our study revealed that the basal activity of cGAS and STING—which have well described roles
253 in sensing of cytosolic DNA including virus replication intermediates [90-92]—underpins the IFN
254 pathway activation in the ACE2(high) cells. What underlies cGAS-STING activation in these cell
255 models is unclear. One plausible explanation is that chromosome and genomic instability
256 commonly present in cancer cell lines [93,94] can trigger cGAS activation [95]. Although mitochondrial
257 damage can also activate cGAS [96,97], we did not find evidence of mitochondrial DNA leakage in
258 the SCC25 cells (not shown).

259 Activation of the cGAS-STING pathway has been shown to contribute to SARS-CoV-2
260 immunopathology and establishment of antiviral defenses [98]. In macrophages, cGAS activation
261 from engulfed DNA of dying endothelial cells near sites of tissue damage can trigger type I IFN
262 responses leading to lung inflammation in COVID-19 patients [99]. In addition, in SARS-CoV-2-
263 infected cells both mitochondrial and nuclear DNA leakage into the cytosol can activate cGAS-

264 STING signaling [99,100]. While STING agonists in uninfected cells can block SARS-CoV-2 infection
265 via triggering type I IFNs [11,101,102], pharmacological inhibition of STING reduces severe lung
266 inflammation induced by SARS-CoV-2 and improves disease outcome in mice [98]. Our study
267 supports the published antiviral functions of cGAS-STING pathway and further expands its role
268 to defining the cellular tropism of SARS-CoV-2 *in vitro*. Healthy gut microbiome-induced cGAS-
269 STING activation at a basal state *in vivo* [60] represents a particularly relevant context for our
270 observations. SARS-CoV-2 can efficiently infect cells within infect gastrointestinal tract *in vitro*
271 [103,104], but it is possible that microbiota-induced activation of the cGAS-STING pathway can limit
272 SARS-CoV-2 replication within the GI tract or its tropism within particular cell subsets therein.
273 Interestingly, STING KO in K18-ACE2 mouse model did not appear to affect host defense and
274 pathology [105]. The use of non-native K18 promoter driving ACE2 overexpression in tissues, which
275 we show can decrease sensitivity to IFN-mediated inhibition, is a possible caveat in this latter
276 study.

277 SARS-CoV-2-encoded proteins including ORF3a, ORF10 and 3CLpro have been shown to
278 antagonize the cGAS-STING pathway largely through inhibition of downstream signaling [106-108].
279 Our study is the first, to our knowledge, to demonstrate that in the primary airway cultures a
280 significant number of productively infected cells lack STING expression (**Fig. 6B, S6A, S6B**). It
281 will be important to determine whether this reduction in STING levels in infected primary airway
282 cells is due to direct antagonism by SARS-CoV-2 proteins via STING degradation. An alternative
283 expression is the preferential infection of cells that lack STING, which has clear implications for
284 the cellular tropism for SARS-CoV-2 in this relevant model system.

285 While our data strongly suggests that cGAS-STING pathway activation underlies the resistance
286 phenotype of multiple ACE2(high) cell models, there were a few exceptions. For example, Detroit
287 562 cells supported only low levels of virus replication upon STING KO which persisted even after
288 ACE2 overexpression. In addition, in spite of successful viral entry (**Fig. 1D, E**), H596 cells did

289 not respond to cGAS-STING ablation and required ectopic ACE2 expression. Moving forward,
290 understanding the molecular basis of these post-entry blocks through comparative analysis of the
291 cell models presented herein can reveal novel cell intrinsic mechanisms that limit SARS-CoV-2
292 replication.

293 IFN signaling leads to the transcriptional upregulation of hundreds of ISGs, many of which are
294 effector molecules that limit virus replication by distinct mechanisms [85,86]. Several studies have
295 reported on ISG screens and individual antiviral properties of ISGs against SARS-CoV-2 [51-
296 53,55,56,109,110]. Whether a dominant ISG or multiple ISGs limit SARS-CoV-2 replication in our cell
297 models remains unknown. Of note, many of the prior ISG screens have been conducted in ACE2
298 overexpressing cells or cell lines of non-airway origin. Our findings demonstrate that ACE2
299 overexpression relieves ISG-mediated restriction of SARS-CoV-2 replication (**Fig. S5B, S5C**). As
300 such, we propose that the ISG(high) cell models that express endogenous levels of ACE2
301 provides a unique, and possibly more physiologically relevant, platform to discover the antiviral
302 activities of ISGs.

303 It is noteworthy that while knockdown of STAT2 and IRF9 enhanced virus replication 2-3 logs,
304 IFNAR knockout had a comparably modest (~10-fold) effect, suggesting that in addition to type I
305 IFNs (i.e. IFN-β), the elevated levels of type III IFNs (i.e. IFN-λ, **Fig. S2D**) may be involved in
306 maintaining the high ISG levels in SCC25 cells. Furthermore, despite efficient knockdown of
307 STAT1, SARS-CoV-2 replication was not restored in SCC25 cells. While it is possible that the
308 residual levels of STAT1 can maintain high ISG expression levels, several studies have
309 established that STAT2 alone can maintain prolonged ISG expression in several cell culture and
310 animal models [111].

311 SARS-CoV-2 encodes numerous non-structural and accessory proteins that can antagonize IFN-
312 mediated innate immune responses. For example nsp1, nsp6, nsp13, ORF3a, M, N, ORF6,

313 ORF7a, ORF7b and ORF8 inhibit IFN signaling [13-20], whereas nsp1, nsp5, nsp6, nsp15, ORF6
314 and ORF7b can block the production of IFN-β [19-21]. Published protein-protein interaction studies
315 provide additional support; SARS-CoV-2 proteins interact with IFN pathway components [112-114]
316 and can antagonize specific ISGs [53]. Given that ISG expression is limited to uninfected bystander
317 cells in both SCC25 STING KO cells and primary airway cultures, our findings suggest that SARS-
318 CoV-2 replication prevents IFN signaling but not IFN production in infected cells. It remains to be
319 determined whether one or more of the abovementioned SARS-CoV-2 proteins is sufficient to
320 block IFN signaling in the cell models presented here.

321 Severe COVID-19 is marked by virus-induced lung damage [115] and a dysregulated immune
322 response [116-119]. Several lines of evidence highlight how IFN-mediated innate immunity is linked
323 to COVID-19 disease severity in humans. For example, severe COVID-19 patients exhibit an
324 impaired type I and III IFN response but a heightened inflammatory response [120,121].
325 Autoantibodies against type I IFNs observed in severe COVID patients may contribute to the
326 observed impairment of innate immunity [122]. In addition, young infants exhibit robust functional
327 antibody responses but restrained IFN-γ production following SARS-CoV-2 infection compared to
328 adults [123]. Therefore, understanding the molecular basis of how SARS-CoV-2 and innate immune
329 responses is critical to our understanding of the complex SARS-CoV-2 pathogenesis *in vivo*. Our
330 study highlights that in addition to expression levels of ACE2, basal activation of the cGAS-STING
331 and IFN pathways can contribute to defining the SARS-CoV-2 cellular tropism. Further dissection
332 of these pathways may lead to the identification of actionable host cell targets that are central to
333 the complex SARS-CoV-2 pathogenesis.

334 **ACKNOWLEDGEMENTS**

335 This work was supported in part by a V Foundation grant (T2014-009) to M.B. Major, a T32
336 training grant (T32CA009547-34) to K.L. We thank the Miner lab for STING CRISPR plasmid and

the Molecular Microbiology Imaging Facility (Wandy L. Beatty) for help with confocal microscopy and data analysis. We thank members of the Lopez, Lenschow, Diamond, Ding and Boon labs for reagents and critical input.

AUTHOR CONTRIBUTIONS

M. P-C., K.M.L., M.B.M., D.G. and S.B.K. conceptualized the study; M. P-C., K.M.L., M.B.M., D.G., S.L.B. and S.B.K. designed the methodology. M. P-C., K.M.L., J.P., J.X., J.E.E., S.M., D.Q.L., Q.W. and S.B.K performed the experiments. R.J. and D.G. performed statistical and bioinformatics analysis. M. P-C., M.B.M., D.G. and S.B.K. wrote the manuscript with input from all the authors.

356 **MATERIALS AND METHODS**

357 ***Cell Culture***

358 All cell lines were maintained in a humidified incubator at 37°C with 5% CO_2 unless otherwise
359 indicated. Cell line identities were validated by short tandem repeat analysis (LabCorp, Genetica
360 Cell Line Testing) and cultures were regularly tested for mycoplasma contamination using the
361 MycoAlert mycoplasma detection kit (Lonza). HEK293T and Calu-3 (ATCC-HTB-55) cells were
362 cultured in Dulbecco's Modified Eagle's Medium (DMEM, Sigma), supplemented with 10% FBS
363 (VWR). Vero CCL-81, Vero E6 and Vero E6-TMPRSS2 (kind gift of Whelan lab [124]) cells were
364 cultured in DMEM, supplemented with 10% FBS and 10 mM HEPES buffer. The A427 (kind gift
365 from Bernard Weissman Lab (UNC)) and Detroit 562 (ATCC-CCL-138) cell lines were cultured in
366 Eagle's Minimum Essential Medium (EMEM, Corning), supplemented with 10% FBS (Sigma), and
367 2 mmol/L L-glutamine (Gibco). The SCC25 (kind gift from the John Hayes Lab (UTHSC) cell line
368 was cultured in DMEM:F12 (Corning) supplemented with 10% FBS (Sigma). The H522 (ATCC-
369 CRL-5810), H596 (ATCC HTB-178), H1299 (ATCC CRL-5803), HCC827 (ATCC CRL-2868), PC-
370 9 (Sigma #90071810), KYSE30 (kind gift from the John Hayes Lab), and OE21 (Sigma #
371 96062201) cell lines were cultured in Roswell Park Memorial Institute (RPMI) 1640 (Corning) with
372 L-glutamine supplemented with 10% FBS (Sigma).

373 Primary human bronchial epithelial cells (HBECs) grown at air-liquid interface (ALI) were
374 processed as follows. Human airway epithelial cells were isolated from surgical excess of
375 tracheobronchial segments of lungs donated for transplantation as previously described and were
376 exempt from regulation by US Department of Health and Human Services regulation 45 Code of
377 Federal Regulations Part 46 [125]. Tracheobronchial cells were expanded in culture, seeded on
378 supported membranes (Transwell; Corning, Inc.), and differentiated using ALI conditions as
379 detailed before using 24-well inserts [126,127].

380 ***Viral Strains***

381 SARS-CoV-2 strain 2019-nCoV/USA-WA1/2020 was obtained from Centers for Disease Control
382 and Prevention (a gift of Natalie Thornburg). The mNeonGreen (mNG) SARS-CoV-2 reporter
383 virus [9] was a gift of Pei-Yong Shi lab, and SARS-CoV-2 Lambda, Iota, Mu, Beta, Epsilon, Delta,
384 Kappa, and Omicron variant isolates were obtained from Dr. Michael S. Diamond. SARS-CoV-2,
385 SARS-CoV-2-mNG and variant isolates were propagated in Vero E6-TMPRSS2 at an MOI of 0.01
386 grown in DMEM (Sigma), supplemented with 2% Fetal Bovine Serum (FBS, VWR) and 10 mM
387 HEPES buffer (Corning). SARS-CoV-2 Omicron variant strain was grown in DMEM supplemented
388 with 1% FBS. After amplification, the viral stocks were titered on Vero-TMPRSS2 cells by plaque
389 assays and sequence confirmed. All experiments involving SARS-CoV-2 were performed in a
390 biosafety level 3 laboratory.

391 ***SARS-CoV-2 infections and focus-forming assay***

392 Cells seeded at 70-80% density were inoculated with virus diluted in cell culture media
393 supplemented with 2% FBS and intermittent rocking for 1 h. Virus inoculum was removed, cells
394 washed with 1x phosphate-buffered saline (PBS) and plated in cell culture media containing 10%
395 FBS. Infections were monitored by focus-forming assay, and RT-qPCR of cell-associated vRNA
396 (N sub-genomic RNA). Briefly, for focus-forming assay, Vero E6-TMPRSS2 cells were inoculated
397 with 10-fold serial dilutions of virus containing supernatants from the panel of airway cell lines,
398 incubated for 1 h at 37°C with intermittent rocking, followed by addition of 2% methylcellulose and
399 2X MEM containing 4% FBS. 30 hours post-infection cells were fixed by 4% paraformaldehyde
400 (PFA) and stained as previously described [124]. Briefly, cells were incubated with CR3022 anti-S
401 antibody (1 ug/mL)[128] overnight followed by anti-human IgG-HRP-conjugated goat secondary
402 antibody (Sigma, 1:500) for 2 h, then foci were visualized with TrueBlue peroxidase substrate
403 (KPL, #5510-0050) and manually counted under the microscope.

404 Prior to infection, HBECs were washed two times with 1× PBS to remove the mucous layer that
405 otherwise can slow down infection. HBECs were inoculated with SARS-CoV-2-mNG in DMEM-
406 supplemented with 2% FBS for two hours in a humidified incubator at 37°C, after which the initial
407 inoculum was removed, cells washed with 1xPBS and maintained at ALI for the duration of the
408 assays. Subsequently, cells were fiixed with 4% paraformaldehyde and subjected to
409 immunofluorescence microscopy as detailed below.

410 ***ACE2 overexpression, lentivirus production and transduction***

411 Cell lines stably expressing human ACE2 were generated by lentiviral transduction as described
412 before [76]. Briefly, lentiviruses were produced in HEK293T cells by polyethyleneimine
413 (Polysciences)-mediated transfection using an pLV-EF1a-IRES-Puro (Addgene Plasmid
414 #85132)-based vector expressing human ACE2, psPAX2 as packaging plasmid (Addgene
415 #12260) and VSV-G expressing envelope plasmid (Addgene #12259). Cell culture supernatants
416 containing lentiviruses were collected and used to transduce SCC25, OE21, Detroit 562, H522
417 and H596 airway cell lines. Two days post transduction, cells were selected for two weeks in 2
418 μg/mL puromycin to generate bulk populations expressing ACE2.

419 ***CRISPR knockout cell lines***

420 ACE2 knockout cell lines were generated as previously stated [76]. In short, lentiviruses were
421 generated in HEK293T cells by transfection of pLentiCRISPRv2 -Puro plasmid containing a single
422 guide RNA (sgRNA) (GTACTGTAGATGGTGCTCAT) (GenScript) targeting ACE2, psPAX2
423 packaging plasmids (Addgene #12260), and pMD2.G plasmid expressing VSV-G (Addgene
424 #12259) in a ratio of 1:1:0.2 respectively using polyethyleneimine. After transduction of PC-9,
425 KYSE30, HCC827, H1299, SCC25, OE21, A427, Detroit 562, and H596 airway cell lines with the
426 resulting lentiviruses, cells were selected in 2 μg /mL puromycin for two weeks.

427 cGAS-STING pathway (i.e. cGAS, STING, TBK1, and IRF3) knockout cell lines were generated
428 similarly by transduction using lentiviral particles generated using pLentiCRISPRv2 -Puro
429 encoding two separate gene-specific sgRNA per target (Table S1), psPAX2, and VSV-G as
430 described above. Following transduction, SCC25 and OE21 cell lines were selected in 2 ug/mL
431 puromycin for at least two weeks. Similarly, for generating STING knockout airway-derived cell
432 lines, we used a lentiviral vector encoding sgRNA (CATATTACATCGGATATCTG) and cells were
433 similarly selected in 2 μg/mL puromycin minimally for two weeks prior to proceeding with SARS-
434 CoV-2 experiments. In all experiments, bulk populations were used for downstream analyses.

435 ***RNA extraction and RT-qPCR***

436 Cell associated RNA was extracted by Trizol following manufacturer's instructions (Thermo-Fisher
437 Scientific) and was subjected to RT-qPCR analysis for viral (*N* sgRNA) or cellular RNAs. SARS-
438 CoV-2 viral RNA was detected by reverse transcription and amplification using the TaqMan RNA-
439 to-CT 1-Step Kit (Thermo Fisher Scientific), utilizing the primers and probe sequences for viral
440 RNAs are as described before [76]. Briefly, reverse transcription was performed at 48 °C for
441 15 minutes, followed by a 2-minute incubation at 95 °C. Amplification was carried out over 50
442 cycles, with each cycle consisting of a 15 second denaturation step at 95 °C, followed by a 1-
443 minute annealing/extension step at 60 °C. The quantification of SARS-CoV-2 N gene RNA copies
444 was determined using a previously published internal RNA standard [129]. To study the type I/III
445 IFN response, cellular RNA was reverse transcribed with High-Capacity cDNA Reverse
446 Transcription kit (Thermo Fisher Scientific) followed by RT-qPCR analysis using PowerUp SYBR
447 Green Master Mix (Applied Biosystems), utilizing ISG-specific primers that were described before
448 [76] and are listed in the Table S2. RNA levels were quantified using the $2^{-\Delta\Delta CT}$ method and
449 normalized relative to *18S rRNA* as the reference target.

450 ***Viral RNA detection by RNAscope***

451 SARS-CoV-2 RNA was detected as described before (41) with minor modifications using the
452 RNAscope Multiplex Fluorescent Reagent Kit v2 (Advanced Cell Diagnostics catalog #323100).
453 One day after attachment on coverslips placed in 24-well plates, cells were infected with SARS-
454 CoV-2 at an MOI of 2 for 1 h, then washed twice with 1x PBS and fresh media was added. Cells
455 were fixed with 4% PFA at 2 hours post infection, dehydrated and stored at -20°C. On the day of
456 detection, cells were rehydrated and incubated in 0.1% Tween in PBS for 10 min and immobilized
457 on slides. Before probing, cells were first treated with hydrogen peroxide (Advanced Cell
458 Diagnostics catalog #322381) and 1:5 diluted protease III (Advanced Cell Diagnostics catalog
459 #322381) each for 10 minutes at room temperature. Immediately after, an anti-sense RNAscope
460 Probe-V-nCoV2019-S (Advanced Cell Diagnostics catalog #848561) targeting SARS-CoV-2
461 positive strand S RNA was allowed to hybridize at 40°C for 2 hr. All consecutive incubations were
462 performed at 40°C unless otherwise indicated. After probe hybridization, Amplifiers (Amp) were
463 added sequentially as follows; Amp 1 for 30 min, followed by Amp 2 for 30 min, and Amp 3 for 15
464 min. Samples were then incubated with detection reagents including horseradish peroxidase
465 (HRP)-C1 for 15 min, diluted Tyramide Signal Amplification (TSA) Vivid Fluorophore 520 (1:1500,
466 Advanced Cell Diagnostics catalog #323271) in TSA buffer (Advanced Cell Diagnostics catalog
467 #322809) for 30 min and HRP blocker for 30 min. Nuclei were stained with DAPI at room
468 temperature for 30 sec. Coverslips were mounted on slides using Prolong Gold Antifade. Images
469 were taken using a Zeiss LSM 880 Airyscan confocal microscope equipped with a 63/1.4 oil-
470 immersion objective.

471 ***Immunofluorescence microscopy***

472 SARS-CoV-2 N protein was visualized in infected cells as before [76]. Briefly, cells grown on
473 coverslips (Neuvitro, #GG-12-1.5-Collagen) were infected with SARS-CoV-2 and fixed with 4%
474 paraformaldehyde. Coverslips were washed with 1X PBS, incubated in 1% bovine serum albumin
475 (BSA) and 10% FBS in PBS containing 0.1% Tween-20 (PBST) at room temperature for 1 h.

476 Samples were then incubated in a primary mouse SARS-CoV-2 nucleocapsid (N) antibody (Sino
477 Biological Inc., Cat # 40588-T62, 1:1000) at 4 °C overnight. After washing with PBST, samples
478 were incubated in a goat anti-mouse secondary antibody conjugated to Alexa Fluor Plus 488
479 (Invitrogen, Cat# A-11029, 1:1000) at room temperature for 1 h. IFIT3, IFIT2 and STING were
480 detected by incubation with a primary rabbit polyclonal IFIT3 antibody (Novus Biologicals NBP2-
481 32500, 1:500), rabbit polyclonal IFIT2 antibody (Novus Biologicals NBP2-15180SS, 1:500) and
482 rabbit polyclonal STING antibody (Proteintech 19851-1-AP, 1:200) respectively as described
483 above followed by incubation with a goat anti-rabbit fluorescent secondary antibody (Invitrogen
484 Goat anti-Rabbit Alexa Fluor Plus 568™, Cat# A-11036, 1:1000 or Invitrogen Goat anti-Rabbit
485 Alexa Fluor™ Plus 647, Catalog # A32733TR, 1:1000). Nuclei were stained with DAPI diluted in
486 PBS at room temperature for 5 min. Finally, coverslips were washed in PBST followed by PBS
487 and then mounted on slides using Prolong Gold Antifade.

488 For confocal microscopy, samples were analyzed with a Zeiss LSM880 laser
489 scanning confocal microscope (Carl Zeiss Inc. Thornwood, NY). The system is equipped with
490 405nm diode, 488nm Argon, 543nm HeNe, and 633nm HeNe lasers. Plan-Apochromat 20X
491 numerical aperture (NA) 0.8), Plan-Apochromat 40X (NA 1.4) DIC oil, and Plan-Apochromat 63X
492 (NA 1.4) DIC oil objectives were used. ZEN black software (version 2.1 SP3) was used for
493 multichannel image acquisition and for obtaining Z stacks with optimal interval and section
494 thickness. The image analysis software Volocity with Visualization module (version 6.3)
495 (PerkinElmer, Waltham, MA) was used for 3-dimensional rendering of Z slices acquired through
496 the depth of the cell monolayers. Colocalization analysis of Z stacks was performed using the
497 Colocalization module of Volocity. For epifluorescence microscopy, images were taken using
498 Leica using either the ×4 or ×20 objective.

499 ***Immunoblotting***

500 Human cell lines were grown to 70% confluence and lysed in 1X RIPA buffer (50mM Tris-HCl pH
501 7.4, 150mM NaCl, 1mM EDTA, 0.1% SDS, 1% NP-40, 0.25% sodium deoxycholate)
502 supplemented with EDTA-free protease inhibitor cocktail (Roche). Proteins were separated by
503 SDS-PAGE on 4-12% Bis-Tris gels, transferred to a nitrocellulose membranes, blocked in
504 Intercept (PBS) blocking buffer (LI-COR) or 5% milk, and incubated with primary antibodies
505 overnight at 4°C. Washed membranes were incubated for 45 min to 1 hour at room temperature
506 in secondary antibody solution (LI-COR IRDye 680, 800; 1:10,000 in 5% milk or Intercept (PBS)
507 blocking buffer), imaged on an Odyssey® CLx scanner, and analyzed using the Image Studio
508 Software. Antibodies were used at the following dilutions: ACE2 (R&D Systems #AF933, 1:200),
509 β-actin (Sigma #A5316, 1:5000 or Santa Cruz Biotech #sc8432, 1:500), Vinculin (Santa Cruz #sc-
510 73614, 1:2000), pSTAT1-Y701 (Cell Signaling #9167, 1:1000), pSTAT1-S727 (Cell Signaling
511 #8826, 1:1000), STAT1 (Cell Signaling #14994, 1:1000), MX1 (Cell Signaling #37849, 1:1000),
512 IFIT1 (Cell Signaling #14769, 1:1000), STING (Cell Signaling #13647S, 1:1000), cGAS (Cell
513 Signaling #15102S, 1:1000), TBK1 (Cell Signaling #38066S, 1:1000), IRF3 (Cell Signaling
514 #4302S, 1:1000), SARS-CoV-2 Nucleocapsid (Sino Biological # 40588-T62, 1;1000 or # 40143-
515 MM05, 1:1000).

516 ***siRNA transfections***

517 siRNAs (Table S3) were reverse-transfected as described before [76]. In brief, 5 pmoles of siRNAs
518 for each target was complexed with 1.5 µL of Lipofectamine RNAiMAX transfection reagent in 50
519 µL of Opti-MEM following manufacturer's recommendations and added in 24-well cell culture
520 dishes. SCC25 cells were then seeded at $1x10^5$ cells/well. At 2-days post-transfection cells were
521 infected with SARS-CoV-2 at an MOI of 2 i.u./cell, and RNA extracted 3 days later by Trizol and
522 processed for RT-qPCR analysis as above. Knockdown efficiency was assessed by RT-qPCR or
523 immunoblotting.

524 ***RNA-seq and single-cell RNA-seq data analysis***

525 For heatmap analysis of the interferon response pathway in our cell line cohort, RNA-seq TPM
526 data for the Cancer Cell Line Encyclopedia (CCLE) was downloaded from the DepMap portal
527 (DepMap Public 18Q3). Gene sets for the interferon response pathway were extracted from
528 MsigDB's lists of HALLMARK_INTERFERON_GAMMA_RESPONSE and
529 HALLMARK_INTERFERON_ALPHA_RESPONSE genes. Hierarchical clustering and figure
530 generation was performed with the ComplexHeatmap R package. For single-cell expression
531 levels in healthy human airways, normalized counts and cell type metadata were downloaded
532 from a publicly available single-cell study [130].

533 ***Statistical Analysis***

534 Generally, experiments were repeated with at least two biological replicates, represented by n.
535 Each plot includes points for individual biological replicates and mean ± SEM error bars unless
536 otherwise specified. GraphPad Prism 9 software was used for statistical analysis. Statistical
537 parameters and details for each experiment are reported in respective figure legends.

538

539 **REFERENCES**

540 1 Carreno, J. M. *et al.* Activity of convalescent and vaccine serum against SARS-CoV-2
541 Omicron. *Nature* **602**, 682-688, doi:10.1038/s41586-022-04399-5 (2022).
542 2 Cele, S. *et al.* Omicron extensively but incompletely escapes Pfizer BNT162b2
543 neutralization. *Nature* **602**, 654-656, doi:10.1038/s41586-021-04387-1 (2022).
544 3 Cameroni, E. *et al.* Broadly neutralizing antibodies overcome SARS-CoV-2 Omicron
545 antigenic shift. *Nature* **602**, 664-670, doi:10.1038/s41586-021-04386-2 (2022).
546 4 Cao, Y. *et al.* Omicron escapes the majority of existing SARS-CoV-2 neutralizing
547 antibodies. *Nature* **602**, 657-663, doi:10.1038/s41586-021-04385-3 (2022).
548 5 Liu, L. *et al.* Striking antibody evasion manifested by the Omicron variant of SARS-CoV-
549 2. *Nature* **602**, 676-681, doi:10.1038/s41586-021-04388-0 (2022).
550 6 Planas, D. *et al.* Considerable escape of SARS-CoV-2 Omicron to antibody
551 neutralization. *Nature* **602**, 671-675, doi:10.1038/s41586-021-04389-z (2022).
552 7 Busnadiego, I. *et al.* Antiviral Activity of Type I, II, and III Interferons Counterbalances
553 ACE2 Inducibility and Restricts SARS-CoV-2. *mBio* **11**, doi:10.1128/mBio.01928-20
554 (2020).
555 8 Lokugamage, K. G. *et al.* Type I Interferon Susceptibility Distinguishes SARS-CoV-2
556 from SARS-CoV. *J Virol* **94**, doi:10.1128/JVI.01410-20 (2020).
557 9 Xie, X. *et al.* An Infectious cDNA Clone of SARS-CoV-2. *Cell Host Microbe* **27**, 841-848
558 e843, doi:10.1016/j.chom.2020.04.004 (2020).
559 10 Vanderheiden, A. *et al.* Type I and Type III Interferons Restrict SARS-CoV-2 Infection of
560 Human Airway Epithelial Cultures. *J Virol* **94**, doi:10.1128/JVI.00985-20 (2020).
561 11 Li, M. *et al.* Pharmacological activation of STING blocks SARS-CoV-2 infection. *Sci*
562 *Immunol* **6**, doi:10.1126/sciimmunol.abi9007 (2021).
563 12 Hatton, C. F. *et al.* Delayed induction of type I and III interferons mediates nasal
564 epithelial cell permissiveness to SARS-CoV-2. *Nat Commun* **12**, 7092,
565 doi:10.1038/s41467-021-27318-0 (2021).
566 13 Sa Ribero, M., Jouvenet, N., Dreux, M. & Nisole, S. Interplay between SARS-CoV-2 and
567 the type I interferon response. *PLoS Pathog* **16**, e1008737,
568 doi:10.1371/journal.ppat.1008737 (2020).
569 14 Lei, X. *et al.* Activation and evasion of type I interferon responses by SARS-CoV-2. *Nat*
570 *Commun* **11**, 3810, doi:10.1038/s41467-020-17665-9 (2020).
571 15 Konno, Y. *et al.* SARS-CoV-2 ORF3b Is a Potent Interferon Antagonist Whose Activity Is
572 Increased by a Naturally Occurring Elongation Variant. *Cell Rep* **32**, 108185,
573 doi:10.1016/j.celrep.2020.108185 (2020).
574 16 Miorin, L. *et al.* SARS-CoV-2 Orf6 hijacks Nup98 to block STAT nuclear import and
575 antagonize interferon signaling. *Proc Natl Acad Sci U S A* **117**, 28344-28354,
576 doi:10.1073/pnas.2016650117 (2020).
577 17 Xia, H. *et al.* Evasion of Type I Interferon by SARS-CoV-2. *Cell Rep* **33**, 108234,
578 doi:10.1016/j.celrep.2020.108234 (2020).
579 18 Setaro, A. C. & Gaglia, M. M. All hands on deck: SARS-CoV-2 proteins that block early
580 anti-viral interferon responses. *Curr Res Virol Sci* **2**, 100015,
581 doi:10.1016/j.crviro.2021.100015 (2021).
582 19 Hayn, M. *et al.* Systematic functional analysis of SARS-CoV-2 proteins uncovers viral
583 innate immune antagonists and remaining vulnerabilities. *Cell Rep* **35**, 109126,
584 doi:10.1016/j.celrep.2021.109126 (2021).
585 20 Li, J. Y. *et al.* The ORF6, ORF8 and nucleocapsid proteins of SARS-CoV-2 inhibit type I
586 interferon signaling pathway. *Virus Res* **286**, 198074,
587 doi:10.1016/j.virusres.2020.198074 (2020).

21 Shemesh, M. *et al.* SARS-CoV-2 suppresses IFNbeta production mediated by NSP1, 5, 6, 15, ORF6 and ORF7b but does not suppress the effects of added interferon. *PLoS Pathog* **17**, e1009800, doi:10.1371/journal.ppat.1009800 (2021).
22 Felgenhauer, U. *et al.* Inhibition of SARS-CoV-2 by type I and type III interferons. *J Biol Chem* **295**, 13958-13964, doi:10.1074/jbc.AC120.013788 (2020).
23 Walls, A. C. *et al.* Structure, Function, and Antigenicity of the SARS-CoV-2 Spike Glycoprotein. *Cell* **181**, 281-292 e286, doi:10.1016/j.cell.2020.02.058 (2020).
24 Letko, M., Marzi, A. & Munster, V. Functional assessment of cell entry and receptor usage for SARS-CoV-2 and other lineage B betacoronaviruses. *Nat Microbiol* **5**, 562-569, doi:10.1038/s41564-020-0688-y (2020).
25 Hoffmann, M. *et al.* SARS-CoV-2 Cell Entry Depends on ACE2 and TMPRSS2 and Is Blocked by a Clinically Proven Protease Inhibitor. *Cell* **181**, 271-280 e278, doi:10.1016/j.cell.2020.02.052 (2020).
26 Zhou, P. *et al.* A pneumonia outbreak associated with a new coronavirus of probable bat origin. *Nature* **579**, 270-273, doi:10.1038/s41586-020-2012-7 (2020).
27 Hikmet, F. *et al.* The protein expression profile of ACE2 in human tissues. *Mol Syst Biol* **16**, e9610, doi:10.15252/msb.20209610 (2020).
28 Aguiar, J. A. *et al.* Gene expression and in situ protein profiling of candidate SARS-CoV-2 receptors in human airway epithelial cells and lung tissue. *Eur Respir J* **56**, doi:10.1183/13993003.01123-2020 (2020).
29 Hamming, I. *et al.* Tissue distribution of ACE2 protein, the functional receptor for SARS coronavirus. A first step in understanding SARS pathogenesis. *J Pathol* **203**, 631-637, doi:10.1002/path.1570 (2004).
30 To, K. F. & Lo, A. W. Exploring the pathogenesis of severe acute respiratory syndrome (SARS): the tissue distribution of the coronavirus (SARS-CoV) and its putative receptor, angiotensin-converting enzyme 2 (ACE2). *J Pathol* **203**, 740-743, doi:10.1002/path.1597 (2004).
31 Zhao, Y. *et al.* Single-cell RNA Expression Profiling of ACE2, The Receptor of SARS-CoV-2. *Am J Respir Crit Care Med*, doi:10.1164/rccm.202001-0179LE (2020).
32 Zou, X. *et al.* Single-cell RNA-seq data analysis on the receptor ACE2 expression reveals the potential risk of different human organs vulnerable to 2019-nCoV infection. *Front Med* **14**, 185-192, doi:10.1007/s11684-020-0754-0 (2020).
33 Qi, F., Qian, S., Zhang, S. & Zhang, Z. Single cell RNA sequencing of 13 human tissues identify cell types and receptors of human coronaviruses. *Biochem Biophys Res Commun* **526**, 135-140, doi:10.1016/j.bbrc.2020.03.044 (2020).
34 Sungnak, W. *et al.* SARS-CoV-2 entry factors are highly expressed in nasal epithelial cells together with innate immune genes. *Nat Med* **26**, 681-687, doi:10.1038/s41591-020-0868-6 (2020).
35 Hou, Y. J. *et al.* SARS-CoV-2 Reverse Genetics Reveals a Variable Infection Gradient in the Respiratory Tract. *Cell* **182**, 429-446 e414, doi:10.1016/j.cell.2020.05.042 (2020).
36 Israelow, B. *et al.* Mouse model of SARS-CoV-2 reveals inflammatory role of type I interferon signaling. *J Exp Med* **217**, doi:10.1084/jem.20201241 (2020).
37 Winkler, E. S. *et al.* SARS-CoV-2 infection of human ACE2-transgenic mice causes severe lung inflammation and impaired function. *Nat Immunol* **21**, 1327-1335, doi:10.1038/s41590-020-0778-2 (2020).
38 Dinnon, K. H., 3rd *et al.* A mouse-adapted model of SARS-CoV-2 to test COVID-19 countermeasures. *Nature* **586**, 560-566, doi:10.1038/s41586-020-2708-8 (2020).
39 Jiang, R. D. *et al.* Pathogenesis of SARS-CoV-2 in Transgenic Mice Expressing Human Angiotensin-Converting Enzyme 2. *Cell* **182**, 50-58 e58, doi:10.1016/j.cell.2020.05.027 (2020).

40 Daly, J. L. *et al.* Neuropilin-1 is a host factor for SARS-CoV-2 infection. *Science* **370**, 861-865, doi:10.1126/science.abd3072 (2020).
41 Cantuti-Castelvetri, L. *et al.* Neuropilin-1 facilitates SARS-CoV-2 cell entry and infectivity. *Science* **370**, 856-860, doi:10.1126/science.abd2985 (2020).
42 Clausen, T. M. *et al.* SARS-CoV-2 Infection Depends on Cellular Heparan Sulfate and ACE2. *Cell* **183**, 1043-1057 e1015, doi:10.1016/j.cell.2020.09.033 (2020).
43 Yan, R. *et al.* Structural basis for the recognition of SARS-CoV-2 by full-length human ACE2. *Science* **367**, 1444-1448, doi:10.1126/science.abb2762 (2020).
44 Amraei, R. *et al.* CD209L/L-SIGN and CD209/DC-SIGN Act as Receptors for SARS-CoV-2. *ACS Cent Sci* **7**, 1156-1165, doi:10.1021/acscentsci.0c01537 (2021).
45 Lu, Q. *et al.* SARS-CoV-2 exacerbates proinflammatory responses in myeloid cells through C-type lectin receptors and Tweety family member 2. *Immunity* **54**, 1304-1319 e1309, doi:10.1016/j.immuni.2021.05.006 (2021).
46 Wang, S. *et al.* AXL is a candidate receptor for SARS-CoV-2 that promotes infection of pulmonary and bronchial epithelial cells. *Cell Res* **31**, 126-140, doi:10.1038/s41422-020-00460-y (2021).
47 Zhu, S. *et al.* Genome-wide CRISPR activation screen identifies candidate receptors for SARS-CoV-2 entry. *Sci China Life Sci*, doi:10.1007/s11427-021-1990-5 (2021).
48 Gu, Y. *et al.* Receptome profiling identifies KREMEN1 and ASGR1 as alternative functional receptors of SARS-CoV-2. *Cell Res*, doi:10.1038/s41422-021-00595-6 (2021).
49 Baggen, J. *et al.* TMEM106B is a receptor mediating ACE2-independent SARS-CoV-2 cell entry. *Cell* **186**, 3427-3442 e3422, doi:10.1016/j.cell.2023.06.005 (2023).
50 Mantlo, E., Bukreyeva, N., Maruyama, J., Paessler, S. & Huang, C. Antiviral activities of type I interferons to SARS-CoV-2 infection. *Antiviral Res* **179**, 104811, doi:10.1016/j.antiviral.2020.104811 (2020).
51 Wickenhagen, A. *et al.* A prenylated dsRNA sensor protects against severe COVID-19. *Science* **374**, eabj3624, doi:10.1126/science.abj3624 (2021).
52 Pfaender, S. *et al.* LY6E impairs coronavirus fusion and confers immune control of viral disease. *Nat Microbiol* **5**, 1330-1339, doi:10.1038/s41564-020-0769-y (2020).
53 Martin-Sancho, L. *et al.* Functional landscape of SARS-CoV-2 cellular restriction. *Mol Cell* **81**, 2656-2668 e2658, doi:10.1016/j.molcel.2021.04.008 (2021).
54 Mac Kain, A. *et al.* Identification of DAXX as a restriction factor of SARS-CoV-2 through a CRISPR/Cas9 screen. *Nat Commun* **13**, 2442, doi:10.1038/s41467-022-30134-9 (2022).
55 Zang, R. *et al.* Cholesterol 25-hydroxylase suppresses SARS-CoV-2 replication by blocking membrane fusion. *Proc Natl Acad Sci U S A* **117**, 32105-32113, doi:10.1073/pnas.2012197117 (2020).
56 Wang, S. *et al.* Cholesterol 25-Hydroxylase inhibits SARS-CoV-2 and other coronaviruses by depleting membrane cholesterol. *EMBO J* **39**, e106057, doi:10.15252/embj.2020106057 (2020).
57 Loske, J. *et al.* Pre-activated antiviral innate immunity in the upper airways controls early SARS-CoV-2 infection in children. *Nat Biotechnol* **40**, 319-324, doi:10.1038/s41587-021-01037-9 (2022).
58 Abt, M. C. *et al.* Commensal bacteria calibrate the activation threshold of innate antiviral immunity. *Immunity* **37**, 158-170, doi:10.1016/j.immuni.2012.04.011 (2012).
59 Di Domizio, J. *et al.* The commensal skin microbiota triggers type I IFN-dependent innate repair responses in injured skin. *Nat Immunol* **21**, 1034-1045, doi:10.1038/s41590-020-0721-6 (2020).
60 Gutierrez-Merino, J., Isla, B., Combes, T., Martinez-Estrada, F. & Maluquer De Motes, C. Beneficial bacteria activate type-I interferon production via the intracellular cytosolic

688 sensors STING and MAVS. *Gut Microbes* **11**, 771-788,
689 doi:10.1080/19490976.2019.1707015 (2020).
690 61 Schaupp, L. *et al.* Microbiota-Induced Type I Interferons Instruct a Poised Basal State of
691 Dendritic Cells. *Cell* **181**, 1080-1096 e1019, doi:10.1016/j.cell.2020.04.022 (2020).
692 62 Lima-Junior, D. S. *et al.* Endogenous retroviruses promote homeostatic and
693 inflammatory responses to the microbiota. *Cell* **184**, 3794-3811 e3719,
694 doi:10.1016/j.cell.2021.05.020 (2021).
695 63 Brown Harding, H. *et al.* Candida albicans extracellular vesicles trigger type I IFN
696 signalling via cGAS and STING. *Nat Microbiol*, doi:10.1038/s41564-023-01546-0 (2024).
697 64 Wypych, T. P., Wickramasinghe, L. C. & Marsland, B. J. The influence of the microbiome
698 on respiratory health. *Nat Immunol* **20**, 1279-1290, doi:10.1038/s41590-019-0451-9
699 (2019).
700 65 Dickson, R. P., Erb-Downward, J. R., Martinez, F. J. & Huffnagle, G. B. The Microbiome
701 and the Respiratory Tract. *Annu Rev Physiol* **78**, 481-504, doi:10.1146/annurev-physiol-
702 021115-105238 (2016).
703 66 Pattaroni, C. *et al.* Early-Life Formation of the Microbial and Immunological Environment
704 of the Human Airways. *Cell Host Microbe* **24**, 857-865 e854,
705 doi:10.1016/j.chom.2018.10.019 (2018).
706 67 Lynch, S. V. & Pedersen, O. The Human Intestinal Microbiome in Health and Disease. *N*
707 *Engl J Med* **375**, 2369-2379, doi:10.1056/NEJMra1600266 (2016).
708 68 Wang, B. *et al.* Alterations in microbiota of patients with COVID-19: potential
709 mechanisms and therapeutic interventions. *Signal Transduct Target Ther* **7**, 143,
710 doi:10.1038/s41392-022-00986-0 (2022).
711 69 Sulaiman, I. *et al.* Microbial signatures in the lower airways of mechanically ventilated
712 COVID-19 patients associated with poor clinical outcome. *Nat Microbiol* **6**, 1245-1258,
713 doi:10.1038/s41564-021-00961-5 (2021).
714 70 Llorens-Rico, V. *et al.* Clinical practices underlie COVID-19 patient respiratory
715 microbiome composition and its interactions with the host. *Nat Commun* **12**, 6243,
716 doi:10.1038/s41467-021-26500-8 (2021).
717 71 Zuo, T. *et al.* Alterations in Fecal Fungal Microbiome of Patients With COVID-19 During
718 Time of Hospitalization until Discharge. *Gastroenterology* **159**, 1302-1310 e1305,
719 doi:10.1053/j.gastro.2020.06.048 (2020).
720 72 Zuo, T. *et al.* Alterations in Gut Microbiota of Patients With COVID-19 During Time of
721 Hospitalization. *Gastroenterology* **159**, 944-955 e948, doi:10.1053/j.gastro.2020.05.048
722 (2020).
723 73 Blanco-Melo, D. *et al.* Imbalanced Host Response to SARS-CoV-2 Drives Development
724 of COVID-19. *Cell* **181**, 1036-1045 e1039, doi:10.1016/j.cell.2020.04.026 (2020).
725 74 Chu, H. *et al.* Comparative replication and immune activation profiles of SARS-CoV-2
726 and SARS-CoV in human lungs: an ex vivo study with implications for the pathogenesis
727 of COVID-19. *Clin Infect Dis*, doi:10.1093/cid/ciaa410 (2020).
728 75 Stukalov, A. *et al.* Multi-level proteomics reveals host-perturbation strategies of SARS-
729 CoV-2 and SARS-CoV. *bioRxiv*, 2020.2006.2017.156455,
730 doi:10.1101/2020.06.17.156455 (2020).
731 76 Puray-Chavez, M. *et al.* Systematic analysis of SARS-CoV-2 infection of an ACE2-
732 negative human airway cell. *Cell Rep* **36**, 109364, doi:10.1016/j.celrep.2021.109364
733 (2021).
734 77 Sampaio, N. G. *et al.* The RNA sensor MDA5 detects SARS-CoV-2 infection. *Sci Rep*
735 **11**, 13638, doi:10.1038/s41598-021-92940-3 (2021).
736 78 Rebendenne, A. *et al.* SARS-CoV-2 triggers an MDA-5-dependent interferon response
737 which is unable to control replication in lung epithelial cells. *J Virol*,
738 doi:10.1128/JVI.02415-20 (2021).

79 Yin, X. *et al.* MDA5 Governs the Innate Immune Response to SARS-CoV-2 in Lung Epithelial Cells. *Cell Rep* **34**, 108628, doi:10.1016/j.celrep.2020.108628 (2021).
80 Kouwaki, T., Nishimura, T., Wang, G. & Oshiumi, H. RIG-I-Like Receptor-Mediated Recognition of Viral Genomic RNA of Severe Acute Respiratory Syndrome Coronavirus-2 and Viral Escape From the Host Innate Immune Responses. *Front Immunol* **12**, 700926, doi:10.3389/fimmu.2021.700926 (2021).
81 Thorne, L. G. *et al.* SARS-CoV-2 sensing by RIG-I and MDA5 links epithelial infection to macrophage inflammation. *EMBO J* **40**, e107826, doi:10.15252/embj.2021107826 (2021).
82 Yang, D. M., Geng, T. T., Harrison, A. G. & Wang, P. H. Differential roles of RIG-I like receptors in SARS-CoV-2 infection. *Mil Med Res* **8**, 49, doi:10.1186/s40779-021-00340-5 (2021).
83 Hoffmann, M. *et al.* Evidence for an ACE2-Independent Entry Pathway That Can Protect from Neutralization by an Antibody Used for COVID-19 Therapy. *mBio* **13**, e0036422, doi:10.1128/mbio.00364-22 (2022).
84 Schoggins, J. W. Recent advances in antiviral interferon-stimulated gene biology. *F1000Res* **7**, 309, doi:10.12688/f1000research.12450.1 (2018).
85 Lazear, H. M., Schoggins, J. W. & Diamond, M. S. Shared and Distinct Functions of Type I and Type III Interferons. *Immunity* **50**, 907-923, doi:10.1016/j.immuni.2019.03.025 (2019).
86 Schoggins, J. W. Interferon-Stimulated Genes: What Do They All Do? *Annu Rev Virol* **6**, 567-584, doi:10.1146/annurev-virology-092818-015756 (2019).
87 Wang, W., Xu, L., Su, J., Peppelenbosch, M. P. & Pan, Q. Transcriptional Regulation of Antiviral Interferon-Stimulated Genes. *Trends Microbiol* **25**, 573-584, doi:10.1016/j.tim.2017.01.001 (2017).
88 Guo, K., Barrett, B. S., Mickens, K. L., Hasenkrug, K. J. & Santiago, M. L. Interferon Resistance of Emerging SARS-CoV-2 Variants. *bioRxiv*, doi:10.1101/2021.03.20.436257 (2021).
89 Ziegler, C. G. K. *et al.* SARS-CoV-2 Receptor ACE2 Is an Interferon-Stimulated Gene in Human Airway Epithelial Cells and Is Detected in Specific Cell Subsets across Tissues. *Cell* **181**, 1016-1035 e1019, doi:10.1016/j.cell.2020.04.035 (2020).
90 Li, Z. *et al.* When STING Meets Viruses: Sensing, Trafficking and Response. *Front Immunol* **11**, 2064, doi:10.3389/fimmu.2020.02064 (2020).
91 Hertzog, J. & Rehwinkel, J. Regulation and inhibition of the DNA sensor cGAS. *EMBO Rep* **21**, e51345, doi:10.15252/embr.202051345 (2020).
92 Ge, Z. & Ding, S. Regulation of cGAS/STING signaling and corresponding immune escape strategies of viruses. *Front Cell Infect Microbiol* **12**, 954581, doi:10.3389/fcimb.2022.954581 (2022).
93 Aguilera, A. & Gomez-Gonzalez, B. Genome instability: a mechanistic view of its causes and consequences. *Nat Rev Genet* **9**, 204-217, doi:10.1038/nrg2268 (2008).
94 Bakhoum, S. F. & Compton, D. A. Chromosomal instability and cancer: a complex relationship with therapeutic potential. *J Clin Invest* **122**, 1138-1143, doi:10.1172/JCI59954 (2012).
95 Mackenzie, K. J. *et al.* cGAS surveillance of micronuclei links genome instability to innate immunity. *Nature* **548**, 461-465, doi:10.1038/nature23449 (2017).
96 Rongvaux, A. *et al.* Apoptotic caspases prevent the induction of type I interferons by mitochondrial DNA. *Cell* **159**, 1563-1577, doi:10.1016/j.cell.2014.11.037 (2014).
97 West, A. P. *et al.* Mitochondrial DNA stress primes the antiviral innate immune response. *Nature* **520**, 553-557, doi:10.1038/nature14156 (2015).

98 Li, H., Zhou, F. & Zhang, L. STING, a critical contributor to SARS-CoV-2 immunopathology. *Signal Transduct Target Ther* **7**, 106, doi:10.1038/s41392-022-00967-3 (2022).
99 Domizio, J. D. *et al.* The cGAS-STING pathway drives type I IFN immunopathology in COVID-19. *Nature* **603**, 145-151, doi:10.1038/s41586-022-04421-w (2022).
100 Zhou, Z. *et al.* Sensing of cytoplasmic chromatin by cGAS activates innate immune response in SARS-CoV-2 infection. *Signal Transduct Target Ther* **6**, 382, doi:10.1038/s41392-021-00800-3 (2021).
101 Humphries, F. *et al.* A diamidobenzimidazole STING agonist protects against SARS-CoV-2 infection. *Sci Immunol* **6**, doi:10.1126/sciimmunol.abi9002 (2021).
102 Liu, W. *et al.* Activation of STING Signaling Pathway Effectively Blocks Human Coronavirus Infection. *J Virol* **95**, doi:10.1128/JVI.00490-21 (2021).
103 Ding, S. & Liang, T. J. Is SARS-CoV-2 Also an Enteric Pathogen With Potential Fecal-Oral Transmission? A COVID-19 Virological and Clinical Review. *Gastroenterology* **159**, 53-61, doi:10.1053/j.gastro.2020.04.052 (2020).
104 Durairajan, S. S. K. *et al.* Gastrointestinal Manifestations of SARS-CoV-2: Transmission, Pathogenesis, Immunomodulation, Microflora Dysbiosis, and Clinical Implications. *Viruses* **15**, doi:10.3390/v15061231 (2023).
105 Marino, G. *et al.* STING is redundant for host defense and pathology of COVID-19-like disease in mice. *Life Sci Alliance* **6**, doi:10.26508/lsa.202301997 (2023).
106 Han, L. *et al.* SARS-CoV-2 ORF10 antagonizes STING-dependent interferon activation and autophagy. *J Med Virol* **94**, 5174-5188, doi:10.1002/jmv.27965 (2022).
107 Su, J. *et al.* SARS-CoV-2 ORF3a inhibits cGAS-STING-mediated autophagy flux and antiviral function. *J Med Virol* **95**, e28175, doi:10.1002/jmv.28175 (2023).
108 Rui, Y. *et al.* Unique and complementary suppression of cGAS-STING and RNA sensing- triggered innate immune responses by SARS-CoV-2 proteins. *Signal Transduct Target Ther* **6**, 123, doi:10.1038/s41392-021-00515-5 (2021).
109 Khan, H. *et al.* TMPRSS2 promotes SARS-CoV-2 evasion from NCOA7-mediated restriction. *PLoS Pathog* **17**, e1009820, doi:10.1371/journal.ppat.1009820 (2021).
110 Soveg, F. W. *et al.* Endomembrane targeting of human OAS1 p46 augments antiviral activity. *Elife* **10**, doi:10.7554/eLife.71047 (2021).
111 Blaszczyk, K. *et al.* The unique role of STAT2 in constitutive and IFN-induced transcription and antiviral responses. *Cytokine Growth Factor Rev* **29**, 71-81, doi:10.1016/j.cytogfr.2016.02.010 (2016).
112 Gordon, D. E. *et al.* A SARS-CoV-2 protein interaction map reveals targets for drug repurposing. *Nature* **583**, 459-468, doi:10.1038/s41586-020-2286-9 (2020).
113 Laurent, E. M. N. *et al.* Global BioID-based SARS-CoV-2 proteins proximal interactome unveils novel ties between viral polypeptides and host factors involved in multiple COVID19-associated mechanisms. *bioRxiv*, 2020.2008.2028.272955, doi:10.1101/2020.08.28.272955 (2020).
114 St-Germain, J. R. *et al.* A SARS-CoV-2 BioID-based virus-host membrane protein interactome and virus peptide compendium: new proteomics resources for COVID-19 research. *bioRxiv*, 2020.2008.2028.269175, doi:10.1101/2020.08.28.269175 (2020).
115 Wu, Z. & McGoogan, J. M. Characteristics of and Important Lessons From the Coronavirus Disease 2019 (COVID-19) Outbreak in China: Summary of a Report of 72314 Cases From the Chinese Center for Disease Control and Prevention. *JAMA*, doi:10.1001/jama.2020.2648 (2020).
116 Wong, L. R. & Perlman, S. Immune dysregulation and immunopathology induced by SARS-CoV-2 and related coronaviruses - are we our own worst enemy? *Nat Rev Immunol*, doi:10.1038/s41577-021-00656-2 (2021).

117 Huang, C. *et al.* Clinical features of patients infected with 2019 novel coronavirus in Wuhan, China. *Lancet* **395**, 497-506, doi:10.1016/S0140-6736(20)30183-5 (2020).
118 Chen, G. *et al.* Clinical and immunological features of severe and moderate coronavirus disease 2019. *J Clin Invest* **130**, 2620-2629, doi:10.1172/JCI137244 (2020).
119 Varga, Z. *et al.* Endothelial cell infection and endotheliitis in COVID-19. *Lancet* **395**, 1417-1418, doi:10.1016/S0140-6736(20)30937-5 (2020).
120 Hadjadj, J. *et al.* Impaired type I interferon activity and inflammatory responses in severe COVID-19 patients. *Science* **369**, 718-724, doi:10.1126/science.abc6027 (2020).
121 Galani, I. E. *et al.* Untuned antiviral immunity in COVID-19 revealed by temporal type I/III interferon patterns and flu comparison. *Nat Immunol* **22**, 32-40, doi:10.1038/s41590-020-00840-x (2021).
122 Bastard, P. *et al.* Autoantibodies against type I IFNs in patients with life-threatening COVID-19. *Science* **370**, doi:10.1126/science.abd4585 (2020).
123 Goenka, A. *et al.* Young infants exhibit robust functional antibody responses and restrained IFN-gamma production to SARS-CoV-2. *Cell Rep Med* **2**, 100327, doi:10.1016/j.xcrm.2021.100327 (2021).
124 Case, J. B. *et al.* Neutralizing Antibody and Soluble ACE2 Inhibition of a Replication-Competent VSV-SARS-CoV-2 and a Clinical Isolate of SARS-CoV-2. *Cell Host Microbe* **28**, 475-485 e475, doi:10.1016/j.chom.2020.06.021 (2020).
125 Horani, A. *et al.* Whole-exome capture and sequencing identifies HEATR2 mutation as a cause of primary ciliary dyskinesia. *Am J Hum Genet* **91**, 685-693, doi:10.1016/j.ajhg.2012.08.022 (2012).
126 You, Y., Richer, E. J., Huang, T. & Brody, S. L. Growth and differentiation of mouse tracheal epithelial cells: selection of a proliferative population. *Am J Physiol Lung Cell Mol Physiol* **283**, L1315-1321, doi:10.1152/ajplung.00169.2002 (2002).
127 Horani, A. *et al.* Establishment of the early cilia preassembly protein complex during motile ciliogenesis. *Proc Natl Acad Sci U S A* **115**, E1221-E1228, doi:10.1073/pnas.1715915115 (2018).
128 Case, J. B., Bailey, A. L., Kim, A. S., Chen, R. E. & Diamond, M. S. Growth, detection, quantification, and inactivation of SARS-CoV-2. *Virology* **548**, 39-48, doi:10.1016/j.virol.2020.05.015 (2020).
129 Shema Mugisha, C., Vuong, H. R., Puray-Chavez, M. & Kutluay, S. B. A facile Q-RT-PCR assay for monitoring SARS-CoV-2 growth in cell culture. *bioRxiv*, doi:10.1101/2020.06.26.174698 (2020).
130 Deprez, M. *et al.* A Single-Cell Atlas of the Human Healthy Airways. *Am J Respir Crit Care Med* **202**, 1636-1645, doi:10.1164/rccm.201911-2199OC (2020).

875 **FIGURE LEGENDS**

876 **Figure 1**. **SARS-CoV-2 replication is blocked at a post-entry stage in a subset of airway-**
877 **derived cell lines that endogenously express ACE2. (A)** The indicated airway-derived cell lines
878 were inoculated with WT SARS-CoV-2 at an MOI: 0.15 i.u./cell. RT-qPCR analysis of cell-
879 associated SARS-CoV-2 N sgRNA (copies/cell) at 4 and 72 hpi is shown. Data show the average
880 of 2 independent experiments, errors bars denote the range. **(B)** Focus forming assay performed
881 on culture supernatants of the indicated cells infected with SARS-CoV-2 for 72 hpi (from panel
882 A). Data show focus forming units per mL (FFU/mL, log transformed) from two independent
883 experiments, error bars show the SEM. **(C)** Polyclonal pools of ACE2 knockout (ACE2-KO) and
884 control cell lines transduced with a non-targeting sgRNA (NT) were infected with WT SARS-CoV-
885 2 at a MOI: 2 i.u./cell. RT-qPCR analysis of cell-associated viral RNA (sgRNA N) at 72 hpi is
886 shown from two biological replicates. Data show the mean, error bars show the SEM, **$p < 0.01$
887 where significance was assessed by multiple unpaired t-tests. **(D)** Polyclonal pools of ACE2 KO
888 and non-targeting control (NT) cell lines were infected with WT SARS-CoV-2 at a MOI:2 i.u./cell.
889 In situ hybridization of incoming viral RNA (green) at 2 hpi was performed as detailed in Methods.
890 Nuclear DAPI staining is shown in blue. **(E)** Quantification of data presented in Panel D. Puncta
891 of SARS-CoV-2 RNA was counted in ~200 cells per cell line from two independent experiments.
892 The average number of RNA puncta per condition is shown in the graph.

893 **Figure 2**. **ACE2(high) airway-derived cell lines that are resistant to SARS-CoV-2 replication**
894 **express high baseline levels of type I IFN pathway genes. (A)** Hierarchical clustering of IFN
895 response pathway RNA expression levels downloaded from CCLE. The heatmap displays z-
896 scored $\log_2$(TPM) values. **(B-E)** RT-qPCR analysis of representative ISGs including *Ifit1, Mx1, Irf9*
897 and *Stat1* in uninfected cells. Expression levels are normalized relative to Calu-3 cells (set to 1).
898 N=2-4 independent biological replicates, error bars denote SEM. **(F)** Immunoblot showing
899 pSTAT1 (Y701 and S727), STAT1, IRF7, IRF9, MX1, IFIT1 and Vinculin levels across airway-

900 derived cell lines (not infected). Blots are representative of two independent experiments. **(G, H)**
901 The indicated airway-derived cell lines were infected with SARS-CoV-2 infected cells at an MOI
902 of 2 i.u./cell and expression of ISGs including *Ifit1* and *Ifit2* in was analyzed by RT-qPCR at 4 and
903 72 hpi. Y-axes indicate ISG fold induction at 72 hpi relative to 4hpi. Data show the mean from n=3
904 independent replicates, errors bars show the SEM.

905 **Figure 3**. **Basally active type I IFN pathway limits SARS-CoV-2 replication in a subset of**
906 **ACE2(high) cells. (A, B)** SCC25, H596, OE21, Detroit 562 and Calu-3 cells were pretreated with
907 1 μM ruxolitinib for 24 hours. *Ifit1 and Mx1* expression was analyzed by RT-qPCR and expression
908 levels are shown relative to untreated Calu-3 cells (set to 1). Data show the mean from n=2-4
909 independent biological replicates, error bars show the SEM. **(C)** SCC25, H596, OE21 and Detroit
910 562 cells were pretreated with DMSO (mock) or 1 μM ruxolitinib for 24 hours and infected with
911 SARS-CoV-2 at a MOI of 2 i.u./cell in presence of DMSO or 1 μM ruxolitinib. RT-qPCR analysis
912 shows cell-associated viral RNA levels at 72 hpi. Data show the mean from n=2 independent
913 replicates, error bars show the SEM. **(D-G)** SCC25 cells transfected with 3 separate siRNAs
914 targeting STAT2 (D), IRF9 (E), STAT1 (G) or a non-targeting control (NT) and polyclonal
915 populations of SCC25 cells knocked out for IFNAR (KO) using two independent sgRNAs or
916 transduced with a non-targeting (NT) control (F) were infected with SARS-CoV-2 at a MOI of 2
917 i.u./cell. Cell-associated viral RNA was analyzed by RT-qPCR at 72 hpi. Y-axes indicate the
918 relative expression ratio between knockdown (KD) or knockout (KO) and the respective NT
919 samples. Data display the mean of 5-6 independent replicates, error bars denote the SEM.

920 **Figure 4. A constitutively active cGAS-STING pathway limits SARS-CoV-2 replication in**
921 **SCC25 cells. (A)** SCC25 cells were transfected with 2 distinct siRNAs targeting the indicated
922 genes or a non-targeting control (NT). 2d post-transfection, cells were infected with SARS-CoV-
923 2 at an MOI of 2 i.u./cell for 72 h. Data show the ratio of cell-associated viral RNA, as assessed

924 by RT-qPCR, between knockdown (KD) and NT samples. Data display the mean of n=2 - 4
925 biological replicates, with error bars representing SEM. **(B)** Polyclonal populations of SCC25 cells
926 knocked out (KO) for cGAS, STING, TBK1, and IRF3 using two separate sgRNAs or transduced
927 with two individual non-targeting (NT) controls were infected with SARS-CoV-2 at MOI: 2 i.u./cell
928 for 72h. RT-qPCR analysis of cell-associated viral N RNA from 4-5 replicates is shown, where
929 error bars show the SEM. ****$p < 0.0001$ significance was assessed by a one-way ANOVA and
930 the Dunnett correction for multiple comparisons. **(C)** Immunoblots show SARS-CoV-2 N, cGAS,
931 STING, TBK1, and IRF3 expression levels in SCC25 cells from panel B. β-actin serves as the
932 loading control. (Representative of n=2). **(D)** Bulk populations of SCC25 STING KO cells were
933 infected with SARS-CoV-2-mNeonGreen (NG) at a MOI:2 i.u./cell. NG-positive cells were
934 enumerated by flow cytometry at 24, 48 and 72 hpi and represented as percentage of total
935 population. Data show the mean of n=2 independent experiments, error bars denote the SEM.**(E)**
936 SCC25 STING KO cells and NT control cells were pretreated with DMSO or 1 uM ruxolitinib for
937 24 hours and infected with SARS-CoV-2-mNG at a MOI:2 i.u./cell. NG-positive cells were
938 enumerated by flow cytometry at 72 hpi and represented as percentage of total population. Data
939 show the mean of n=4 independent experiments, error bars denote the SEM. **$p< 0.01$ where
940 significance was assessed by 2-way ANOVA and Šidák multiple test correction.

941 **Figure 5**. **Impact of an active cGAS - STING pathway-mediated vs. SARS-CoV-2-induced**
942 **type-I IFN activation on SARS-CoV-2 replication. (A)** Expression levels of ISGs *Isg15, Ifit1,*
943 *Ifit2, Ifit3 and Irf7* were assessed by RT-qPCR in uninfected polyclonal populations of SCC25 cells
944 knocked out (KO) for cGAS and STING or transduced with a non-targeting (NT) control.
945 Expression levels were normalized relative to NT control (set to 1). N=2-3 independent biological
946 replicates, error bars show SEM. **(B)** Uninfected polyclonal populations of STING KO or NT
947 SCC25 cells were subjected to immunostaining for IFIT3. IFIT3 label (in red) and nuclei (DAPI, in
948 blue) observed under 4X objective by epifluorescence microscopy. Scale bars show 500 μM,

949 (representative of n=2). **(C)** Relative expression of ISGs including *Isg15, Ifit1, Ifit2, Ifit3 and Irf7* in
950 SCC25 STING KO or NT control cells, uninfected or infected with SARS-CoV-2 at a MOI of 2
951 i.u./cell. Cells were collected at 72 hpi and ISG expression analyzed by RT-qPCR. Data show the
952 fold induction of ISGs in infected over uninfected cells from n=3 biological replicates, errors bars
953 show the SEM. **(D, E)** SCC25 STING KO or NT control cells were infected with SARS-CoV-2 at
954 an MOI of 2 i.u./cell. Immunofluorescence detection for IFIT3 expression (in red) and SARS-CoV-
955 2 nucleocapsid (N) viral protein (in green), and cellular nuclei (DAPI, in blue) at 72hpi from a
956 representative experiment (n = 2) are shown. Images were collected with an epifluorescence
957 microscope, 4X objective (D) or Zeiss LSM 880 Airyscan confocal microscope equipped with a
958 ×63/1.4 objective (E) as detailed in Methods. Scale bars = 250 μM (D) or 10 μM (E).

959 **Figure 6. Analysis of ISG and STING expression in SARS-CoV-2-infected primary human**
960 **airway epithelial cell s(hTEC) grown at ALI. (A)** hTECs from two donors grown at ALI were
961 infected with SARS-CoV-2-mNG at an MOI of 2 i.u./cell and fixed at 72 hpi. Immunofluorescence
962 detection for IFIT2 expression (in red), mNG (in green), and cellular nuclei (DAPI, in blue) is
963 shown. Images were analyzed by confocal microscopy with a ×40/1.4 objective. Scale bars = 50
964 μM, (representative of n=2). **(B)** hTECs from two donors were infected with SARS-CoV-2-mNG
965 at an MOI of 2 i.u./cell as in (A) and stained for STING (in red) and SARS-CoV-2 N (in green),
966 and cellular nuclei (DAPI, in blue). Images were analyzed by confocal microscopy with a ×20
967 objective. Scale bars = 50 μM, (representative of n=2).

968 **Figure 7: Expression profiles of cGAS, STING and representative ISGs in the healthy**
969 **human airways.** Normalized counts and cell type metadata were downloaded from a publicly
970 available single-cell study [130]. Detection frequency represents that percentage of cells with > 0
971 counts for respective gene. Bar plots display the average normalized expression for a gene within
972 a cell type. For the gene set representing the interferon alpha Gene Ontology term, normalized

973 expression levels were summed for all genes in the set prior to computing detection frequencies
974 and average expression.
975
976
977
978
979
980
981
982
983
984
985
986
987
988
989
990

991 **SUPPLEMENTARY FIGURE LEGENDS**

992 **Figure S1: Analysis of SARS-CoV-2 replication in a panel of airway-derived cell lines that**
993 **endogenously express ACE2. (A)** RNA expression of SARS-CoV-2 viral entry factors
994 downloaded from the Cancer Cell Line Encyclopedia (CCLE). The heatmap displays log2(TPM)
995 values. **(B)** Airway-derived cell lines were infected at a MOI: 2 i.u./cell and cell lysates were
996 analyzed by immunoblotting using anti-SARS-CoV-2 N and anti-actin antibodies at 3 dpi.
997 Immunoblots are representative of two independent replicates.

998 **Figure S2: Expression levels of IFN pathway genes in uninfected and infected cell lines.**
999 **(A)** Calu-3 cells were pretreated for 6 or 24 hours or treated at the indicated time points post-
1000 infection with 1000 U/mL IFN-α and infected with SARS-CoV-2 at MOI: 2 i.u./cell. RT-qPCR
1001 analysis of cell-associated SARS-CoV-2 N sgRNA (copies/cell) at 72 hpi is shown. Data show the
1002 average of 4 biological replicates, errors bars denote the SD. **(B, C)** RT-qPCR analysis of
1003 representative ISGs including *Ifit2 and Isg15* in uninfected cells. Expression levels are normalized
1004 relative to Calu-3 cells (set to 1). N=2-4 independent biological replicates, error bars denote SEM.
1005 **(D)** RNA expression of IFNs was downloaded from the Cancer Cell Line Encyclopedia (CCLE).
1006 The heatmap displays log2(TPM) values. **(E-H)** The indicated airway-derived cell lines were
1007 infected with SARS-CoV-2 infected cells at an MOI of 2 i.u./cell and expression of ISGs including
1008 *Mx1, Isg15, Ifit3 and Irf7* in was analyzed by RT-qPCR at 4 and 72 hpi. Y-axes indicate ISG fold
1009 induction at 72 hpi relative to 4hpi. Data show the mean from n=3 independent replicates, errors
1010 bars show the SEM.

1011 **Figure S3. Basally active type I IFN pathway limits SARS-CoV-2 replication in a subset of**
1012 **ACE2(high) cells. (A-D)** SCC25, H596, OE21, Detroit 562 and Calu-3 cells were pretreated with
1013 1 μM ruxolitinib for 24 hours. *Ifit2, Isg15, Irf9 and Stat1* expression was analyzed by RT-qPCR
1014 and expression levels are shown relative to untreated Calu-3 cells (set to 1). Data show the mean

1015 from n=2-4 independent biological replicates, error bars show SEM. **(E-G)** Expression levels of
1016 *Stat1, Stat2 and Irf9* were assessed by RT-qPCR in SCC25 cells that were transfected with 3
1017 separate siRNAs targeting STAT1, STAT2 and IRF9 respectively or a non-targeting control (NT)
1018 and infected with SARS-CoV-2 as in Fig. 3. Data display the mean of 3-4 biological replicates,
1019 error bars show SEM. **(H)** SCC25 cells were transfected with 3 separate siRNAs targeting STAT1
1020 or a non-targeting control (NT) and infected with SARS-CoV-2 WT at an MOI of 2 i.u./cell for 72
1021 h. Immunoblots show STAT1, actin (control) and SARS-CoV-2 N expression (representative of
1022 n=2).

1023 **Figure S4. A constitutively active cGAS-STING pathway limits SARS-CoV-2 replication in**
1024 **a subset of ACE2(high) airways cell lines. (A)** Polyclonal populations of OE21 cells knocked
1025 out (KO) for cGAS, STING, TBK1 and IRF3 using two separate sgRNAs or transduced with two
1026 individual non-targeting (NT) controls were infected with SARS-CoV-2 at MOI: 2 i.u./cell. RT-
1027 qPCR analysis of cell-associated viral N RNA show copies per cell from 4 independent
1028 experiments where error bars show SEM. *p<0.05, **p<0.01, ***p<0.001, ****p <0.0001 by one-
1029 way ANOVA and the Dunnett correction for multiple comparisons. **(B)** Panel of airway-derived
1030 cell lines knocked out (KO) for STING or transduced with a non-targeting (NT) control were
1031 infected with SARS-CoV-2 at a MOI: 2 i.u./cell. RT-qPCR analysis of cell-associated viral RNA
1032 (copies/cell) at 72 hpi in NT vs. STING KO cells is displayed. Data show the average of 2
1033 biological replicates, where errors bars indicate the SEM. **(C)** STING immunoblot of the panel of
1034 airway-derived cell lines knocked out (KO) for STING or transduced with a non-targeting control
1035 (NT). β-actin serves as the loading control. Immunoblots are representative of two independent
1036 replicates. **(D)** Bulk populations of SCC25 STING CRISPR cells were infected with mNeonGreen
1037 (NG) reporter SARS-CoV-2 at a MOI:2 i.u./cell. Percentage of NG-positive cells was determined
1038 by flow cytometry at 24, 48 and 72 hpi. Plots are representative of n=2 independent replicates.

1039 **Figure S5. Impact of an active cGAS - STING pathway-mediated vs. SARS-CoV-2-induced**
1040 **type-I IFN activation on SARS-CoV-2 replication. (A)** Bulk populations of SCC25 STING KO
1041 cells were infected with SARS-CoV-2 at a MOI:2 i.u./cell. Percentage of SARS-CoV-2
1042 nucleocapsid (NP) -positive cells (green) and IFIT3 (red) was determined by flow cytometry at 72
1043 hpi. Data show the mean of 4 biological replicates, error bars denote the SEM. **(B)** Indicated cell
1044 lines ectopically expressing ACE2 were infected at a MOI: 0.1 i.u./cell with SARS-CoV-2 WT. RT-
1045 qPCR for cell-associated SARS-CoV-2 RNA at 2-3 and 24 hpi is shown from n=2 replicates. Data
1046 show the mean, error bars denote SEM. **(C)** Airway-derived cell lines ectopically expressing ACE2
1047 were pretreated with 1 μM ruxolitinib or mock for 24 hours and infected with SARS-CoV-2 at a
1048 MOI: 0.1 i.u./cell. RT-qPCR for cell-associated SARS-CoV-2 RNA at 2-3 and 24 hpi is shown from
1049 n=2 replicates. Data show the mean, error bars denote SEM. **(D)** SCC25 cells were pretreated
1050 with 1 μM ruxolitinib or DMSO for 24 hours and infected with SARS-CoV-2 Variants of Concern
1051 (VOC) at a MOI: 2 i.u./cell. RT-qPCR analysis shows cell-associated viral RNA levels at 72 hpi.
1052 Data show the mean from n=2 independent experiments, error bars show SEM.

1053 **Figure S6. Analysis of IFIT2 and STING expression in SARS-CoV-2 infected primary human**
1054 **airway epithelial cells. (A, B)** Pearson's correlation (A) and Mander's overlap (B) coefficient
1055 derived from experiments presented in Fig. 6. Colocalization analysis of Z stacks was performed
1056 using the Colocalization module of Volocity from 5-8 separate Z-stacks. Individual numbers
1057 plotted display the corresponding values from each Z-stack for each Donor. (C) STING (in red)
1058 and cellular nuclei (DAPI, in blue) immunostaining in the uninfected hTEC donors presented in
1059 Fig. 6B. **(D)** SCC25 WT and polyclonal STING-KO cells stained with STING antibody (in red) and
1060 cellular nuclei (DAPI, in blue). Images were analyzed by epifluorescence microscopy with a ×20
1061 objective. Scale bars = 100 μM.

1062

1063

1064

1065 **Table S1 sgRNA sequences**

	Target	sgRNA	Reference
1	cGAS-gRNA1 (cGAS-1)	ATCCCTCCGTACAAAAAGGG	This paper
2	cGAS-gRNA2 (cGAS-2)	AGACTCGGTGGGATCCATCG	This paper
3	STING-gRNA1 (STING-1)	CATATTACATCGGATATCTG	This paper
4	STING-gRNA2 (STING-2)	CACCGCATTACAACAACCTGCTACG	This paper
5	TBK1-gRNA1 (TBK1-1)	ACAGTGTATAAACTCCCACA	This paper
6	TBK1-gRNA2 (TBK1-2)	AAATATCATGCGTGTTATAG	This paper
7	IRF3-gRNA1 (IRF3-1)	CCACTGGTGCATATGTTCCC	This paper
8	IRF3-gRNA2 (IRF3-2)	AGAAGGGTTGCGTTTAGCAG	This paper
9	IFNAR-gRNA1 (IFNAR-1)	CACCGGTACATTGTATAAAGACCAC	This paper
10	IFNAR-gRNA2 (IFNAR-2)	CACCGACATGACCTTTCAAGTTCAG	This paper

1066

1067

1068

1069

1070

1071 **Table S2 Primer sequences**

	Oligo Target	Oligo Sequence	Reference
1	SARS-CoV-2 NP -F	5’ ATGCTGCAATCGTGCTACAA 3’	75
2	SARS-CoV-2 NP -R	5’ GACTGCCGCCTCTGCTC 3’	75
3	IFIT1 (ISG56) -F	5’ CCTCCCTGGAAAATCTAGGCTCT 3’	75
4	IFIT1 (ISG56) -R	5’ GTAAAGTGACATCTCAATTGCTCCAGAC 3’	75
5	IFIT2 (ISG54) -F	5’ AGCTGAGAATTGCACTGCAACCATG 3’	75
6	IFIT2 (ISG54) -R	5’ CTCCATCAAGTTCCAGGTGAAATGGC 3’	75
7	IFIT3 -F	5’ GGGCAGTCATGAGTGAGGTC 3’	This paper
8	IFIT3 -R	5’ AAGTTCCAGGTGAAATGGCA 3’	This paper
9	ISG15 -F	5’ CACAGCCCACAGCCCACAG 3’	75
10	ISG15 -R	5’ GCTCAGGGACACCTGGAATTCG 3’	75
11	MX1 -F	5’ CACTGCGAGGAGATCGGTTC 3’	75
12	MX1 -R	5’ CTGTTCTCCTGCACCTCCTTG 3’	75
13	IRF7 -F	5’ GTCCTGGTGAAGCTGGAACC 3’	This paper

14	IRF7 -R	5’ CAGGGAAGACACACCCTCAC 3’	This paper
15	IRF9 -F	5’ GCCCTACAAGGTGTATCAGTTG 3’	This paper
16	IRF9 -R	5’ TGCTGTCGCTTTGATGGTACT 3’	This paper
17	STAT1 -F	5’ GCTCGTTTGTGGTGGAAAGAC 3’	This paper
18	STAT1 -R	5’ TCTCTCATTCACATCTCTCAACTT 3’	This paper
19	STAT2 -F	5’ CCAGCTTTACTCGCACAGC 3’	This paper
20	STAT2 -R	5’ AGCCTTGGAATCATCACTCCC 3’	This paper
21	Human 18S rRNA -F	5’ CCGCAGCTAGGAATAATGGA 3’	75
22	Human 18S rRNA -R	5’ CGGTCCAAGAATTTCACCTC 3’	75

1072

1073

1074

1075

1076

1077

1078

1079

1080

1081

1082 **Table S3 siRNA information**

	Target	Source	Identifier
1	siTLR3 - 1	Ambion by Life Technologies	s236
2	siTLR3 – 2	Ambion by Life Technologies	s235
3	siTLR7 - 1	Ambion by Life Technologies	s27842
4	siTLR7 - 1	Ambion by Life Technologies	s27843
5	siTLR8 - 1	Ambion by Life Technologies	s27921
6	siTLR8 - 2	Ambion by Life Technologies	s27920
7	siTLR9 - 1	Ambion by Life Technologies	s28873
8	siTLR9 - 2	Ambion by Life Technologies	s28872
9	siRIG-I - 1	Ambion by Life Technologies	s223616
10	siRIG-I - 2	Ambion by Life Technologies	s223615
11	siMDA5 - 1	Ambion by Life Technologies	s34499
12	siMDA5 - 2	Ambion by Life Technologies	s34500
13	siLPG2 - 1	Ambion by Life Technologies	s35594

14	siLPG2 - 2	Ambion by Life Technologies	s35595
15	siMyD88 - 1	Ambion by Life Technologies	s9137
16	siMyD88 - 2	Ambion by Life Technologies	s9138
17	siTRIF – 1	Ambion by Life Technologies	s45114
18	siTRIF - 2	Ambion by Life Technologies	s531858
19	siMAVS - 1	Ambion by Life Technologies	s33179
20	siMAVS – 2	Ambion by Life Technologies	s33180
21	siNOD2 - 1	Ambion by Life Technologies	s533471
22	siNOD2 - 2	Ambion by Life Technologies	s34485
23	siNLRP1 - 1	Ambion by Life Technologies	s22520
24	siNLRP1 - 2	Ambion by Life Technologies	s22521
25	siNLRP1 - 3	Ambion by Life Technologies	s22522
26	siNLRP3 - 1	Ambion by Life Technologies	s534395
27	siNLRP3 - 2	Ambion by Life Technologies	s41556
28	siNLRC5 - 1	Ambion by Life Technologies	s38591
29	siNLRC5 - 2	Ambion by Life Technologies	s38592
30	siSTING - 1	Ambion by Life Technologies	s50644

31	siSTING - 2	Ambion by Life Technologies	s226307
33	siSTAT1 - 1	Ambion by Life Technologies	s277
34	siSTAT1 - 2	Ambion by Life Technologies	s278
35	siSTAT1 - 3	Ambion by Life Technologies	s279
36	siSTAT2 - 1	Ambion by Life Technologies	s13528
37	siSTAT2 - 2	Ambion by Life Technologies	s13529
38	siSTAT2 - 3	Ambion by Life Technologies	s13530
39	siIRF9 - 1	Ambion by Life Technologies	s20290
40	siIRF9 - 2	Ambion by Life Technologies	s20291
41	siIRF9 - 3	Ambion by Life Technologies	s20292

1083

1084

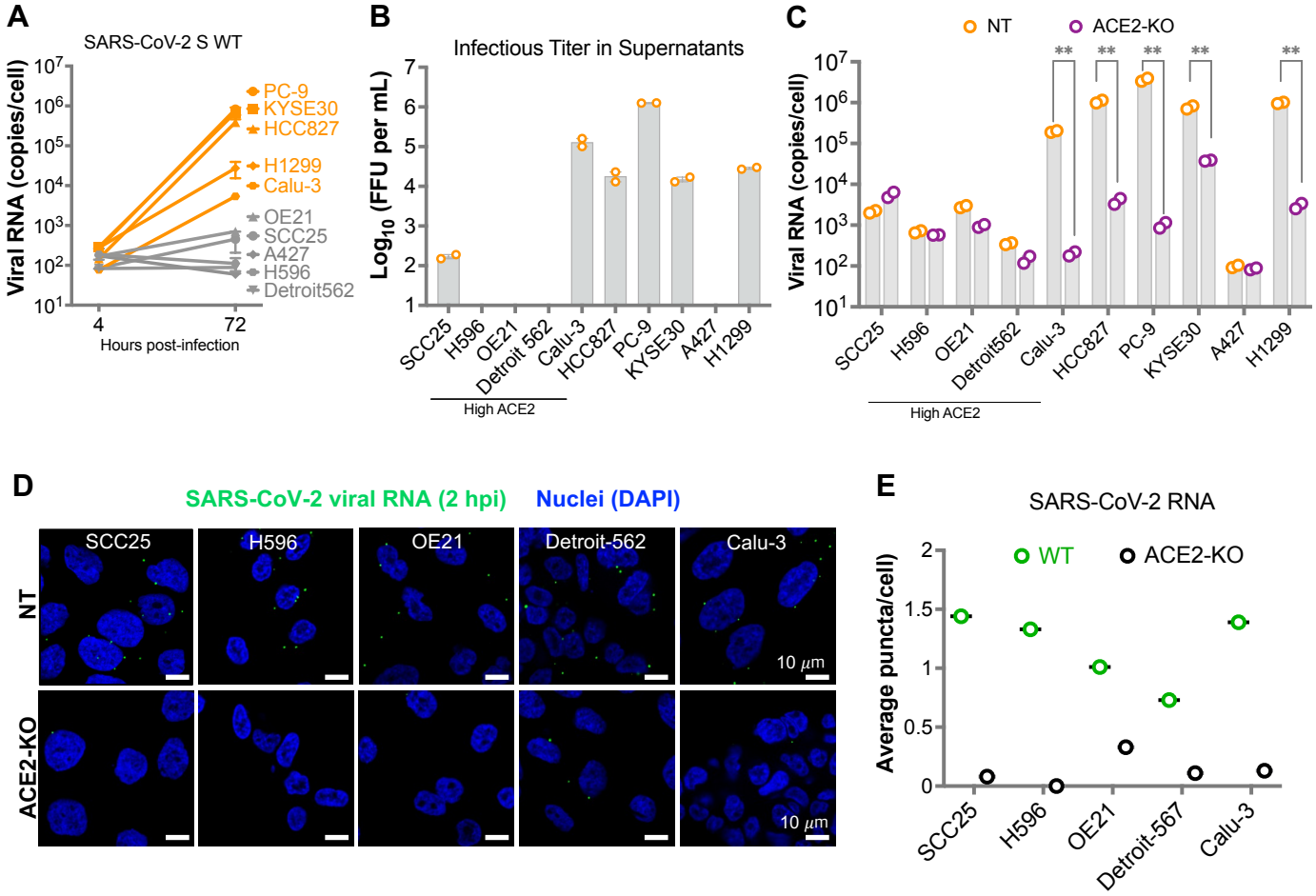

Figure 1. **SARS-CoV-2 replication is blocked at a post-entry stage in a subset of airway-derived cell lines that endogenously express ACE2. (A)** The indicated airway-derived cell lines were inoculated with WT SARS-CoV-2 at an MOI: 0.15 i.u./cell. RT-qPCR analysis of cell-associated SARS-CoV-2 N sgRNA (copies/cell) at 4 and 72 hpi is shown. Data show the average of 2 independent experiments, errors bars denote the range. **(B)** Focus forming assay performed on culture supernatants of the indicated cells infected with SARS-CoV-2 for 72 hpi (from panel A). Data show focus forming units per mL (FFU/mL, log transformed) from two independent experiments, error bars show the SEM. **(C)** Polyclonal pools of ACE2 knockout (ACE2-KO) and control cell lines transduced with a non-targeting sgRNA (NT) were infected with WT SARS-CoV-2 at a MOI: 2 i.u./cell. RT-qPCR analysis of cell-associated viral RNA (sgRNA N) at 72 hpi is shown from two biological replicates. Data show the mean, error bars show the SEM, **p< 0.01 where significance was assessed by multiple unpaired t-tests. **(D)** Polyclonal pools of ACE2 KO and non-targeting control (NT) cell lines were infected with WT SARS-CoV-2 at a MOI:2 i.u./cell. In situ hybridization of incoming viral RNA (green) at 2 hpi was performed as detailed in Methods. Nuclear DAPI staining is shown in blue. **(E)** Quantification of data presented in Panel D. Puncta of SARS-CoV-2 RNA was counted in ~200 cells per cell line from two independent experiments. The average number of RNA puncta per condition is shown in the graph.

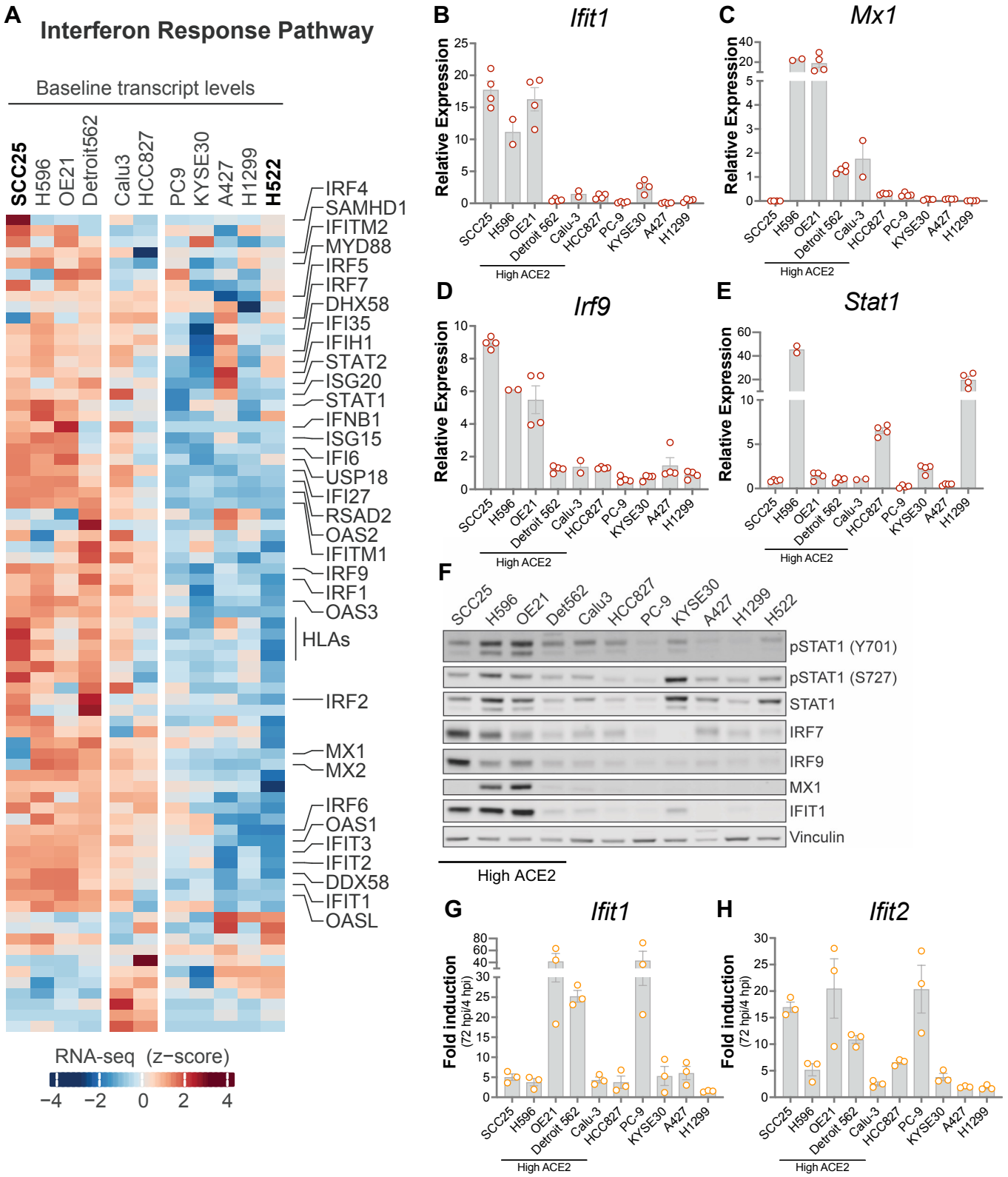

Figure 2. **ACE2(high) airway-derived cell lines that are resistant to SARS-CoV-2 replication express high baseline levels of type I IFN pathway genes. (A)** Hierarchical clustering of IFN response pathway RNA expression levels downloaded from CCLE. The heatmap displays z-scored $\log_2$(TPM) values. **(B-E)** RT-qPCR analysis of representative ISGs including *Ifit1, Mx1, Irf9* and *Stat1* in uninfected cells. Expression levels are normalized relative to Calu-3 cells (set to 1). N=2-4 independent biological replicates, error bars denote SEM. **(F)** Immunoblot showing pSTAT1 (Y701 and S727), STAT1, IRF7, IRF9, MX1, IFIT1 and Vinculin levels across airway-derived cell lines (not infected). Blots are representative of two independent experiments. **(G, H)** The indicated airway-derived cell lines were infected with SARS-CoV-2 infected cells at an MOI of 2 i.u./cell and expression of ISGs including *Ifit1* and *Ifit2* in was analyzed by RT-qPCR at 4 and 72 hpi. Y-axes indicate ISG fold induction at 72 hpi relative to 4hpi. Data show the mean from n=3 independent replicates, errors bars show the SEM.

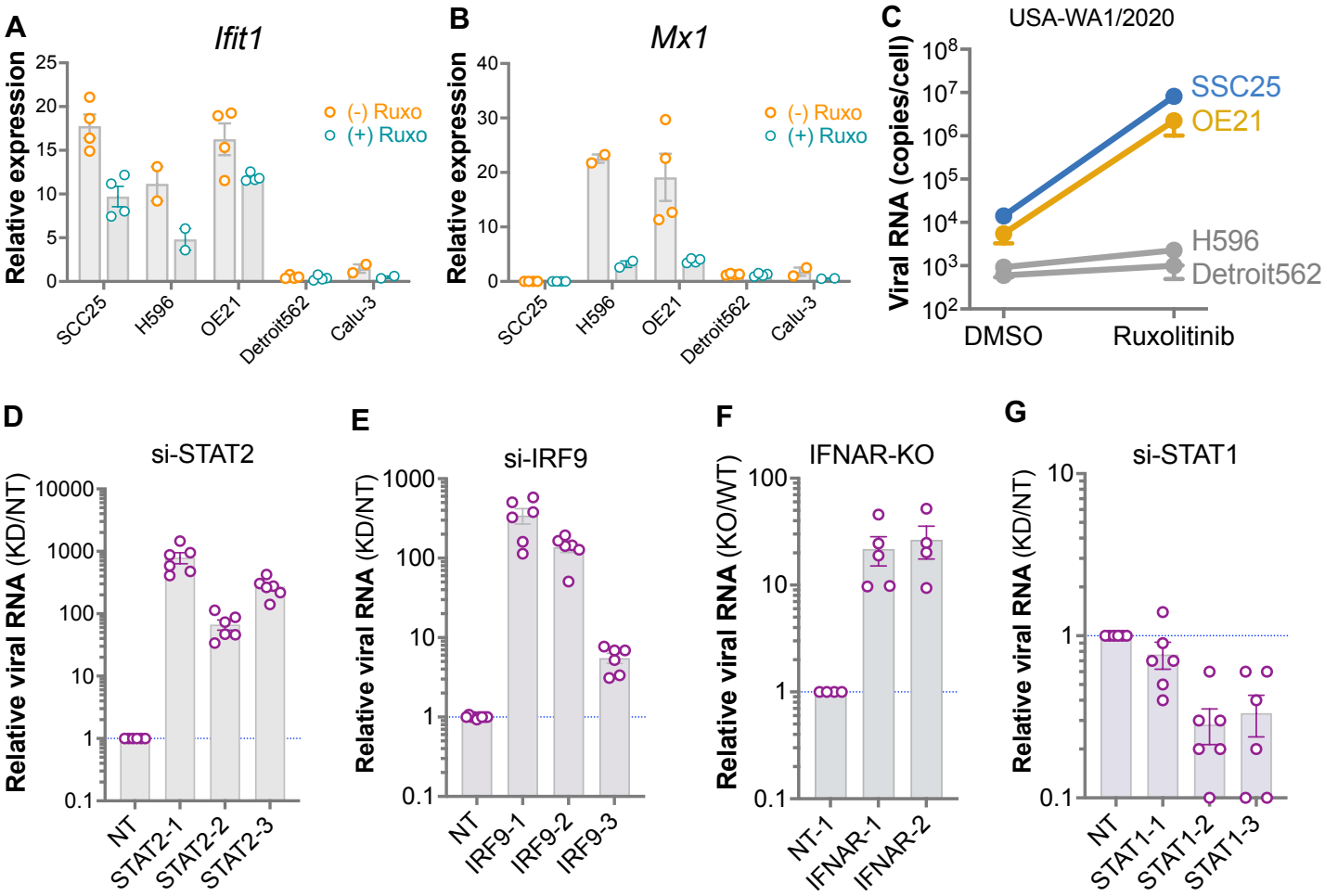

Figure 3. **Basally active type I IFN pathway limits SARS-CoV-2 replication in a subset of ACE2(high) cells. (A, B)** SCC25, H596, OE21, Detroit 562 and Calu-3 cells were pretreated with 1 μM ruxolitinib for 24 hours. *Ifit1 and Mx1* expression was analyzed by RT-qPCR and expression levels are shown relative to untreated Calu-3 cells (set to 1). Data show the mean from n=2-4 independent biological replicates, error bars show the SEM. **(C)** SCC25, H596, OE21 and Detroit 562 cells were pretreated with DMSO (mock) or 1 μM ruxolitinib for 24 hours and infected with SARS-CoV-2 at a MOI of 2 i.u./cell in presence of DMSO or 1 μM ruxolitinib. RT-qPCR analysis shows cell-associated viral RNA levels at 72 hpi. Data show the mean from n=2 independent replicates, error bars show the SEM. **(D-G)** SCC25 cells transfected with 3 separate siRNAs targeting STAT2 (D), IRF9 (E), STAT1 (G) or a non-targeting control (NT) and polyclonal populations of SCC25 cells knocked out for IFNAR (KO) using two independent sgRNAs or transduced with a non-targeting (NT) control (F) were infected with SARS-CoV-2 at a MOI of 2 i.u./cell. Cell-associated viral RNA was analyzed by RT-qPCR at 72 hpi. Y-axes indicate the relative expression ratio between knockdown (KD) or knockout (KO) and the respective NT samples. Data display the mean of 5-6 independent replicates, error bars denote the SEM.

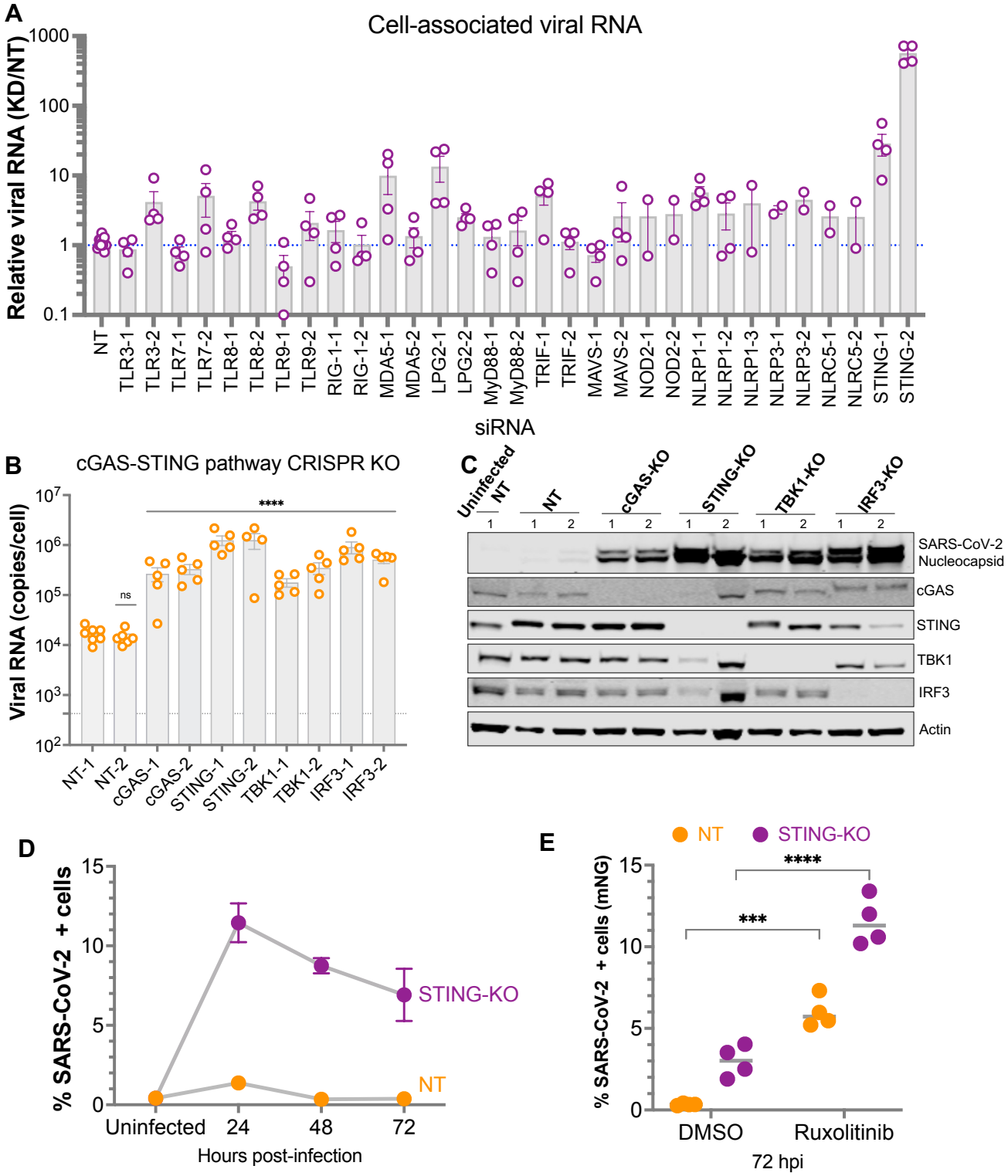

Figure 4. A constitutively active cGAS-STING pathway limits SARS-CoV-2 replication in SCC25 cells. (A) SCC25 cells were transfected with 2 distinct siRNAs targeting the indicated genes or a non-targeting control (NT). 2d post-transfection, cells were infected with SARS-CoV-2 at an MOI of 2 i.u./cell for 72 h. Data show the ratio of cell-associated viral RNA, as assessed by RT-qPCR, between knockdown (KD) and NT samples. Data display the mean of n=2 - 4 biological replicates, with error bars representing SEM. **(B)** Polyclonal populations of SCC25 cells knocked out (KO) for cGAS, STING, TBK1, and IRF3 using two separate sgRNAs or transduced with two individual non-targeting (NT) controls were infected with SARS-CoV-2 at MOI: 2 i.u./cell for 72h. RT-qPCR analysis of cell-associated viral N RNA from 4-5 replicates is shown, where error bars show the SEM. ****$p < 0.0001$ significance was assessed by a one-way ANOVA and the Dunnett correction for multiple comparisons. (legend continued on the next page)

Figure 4 (cont'ed)

(C) Immunoblots show SARS-CoV-2 N, cGAS, STING, TBK1, and IRF3 expression levels in SCC25 cells from panel B. β-actin serves as the loading control. (Representative of n=2). **(D)** Bulk populations of SCC25 STING KO cells were infected with SARS-CoV-2-mNeonGreen (NG) at a MOI:2 i.u./cell. NG-positive cells were enumerated by flow cytometry at 24, 48 and 72 hpi and represented as percentage of total population. Data show the mean of n=2 independent experiments, error bars denote the SEM.**(E)** SCC25 STING KO cells and NT control cells were pretreated with DMSO or 1 uM ruxolitinib for 24 hours and infected with SARS-CoV-2-mNG at a MOI:2 i.u./cell. NG-positive cells were enumerated by flow cytometry at 72 hpi and represented as percentage of total population. Data show the mean of n=4 independent experiments, error bars denote the SEM. **$p < 0.01$ where significance was assessed by 2-way ANOVA and Šidák multiple test correction.

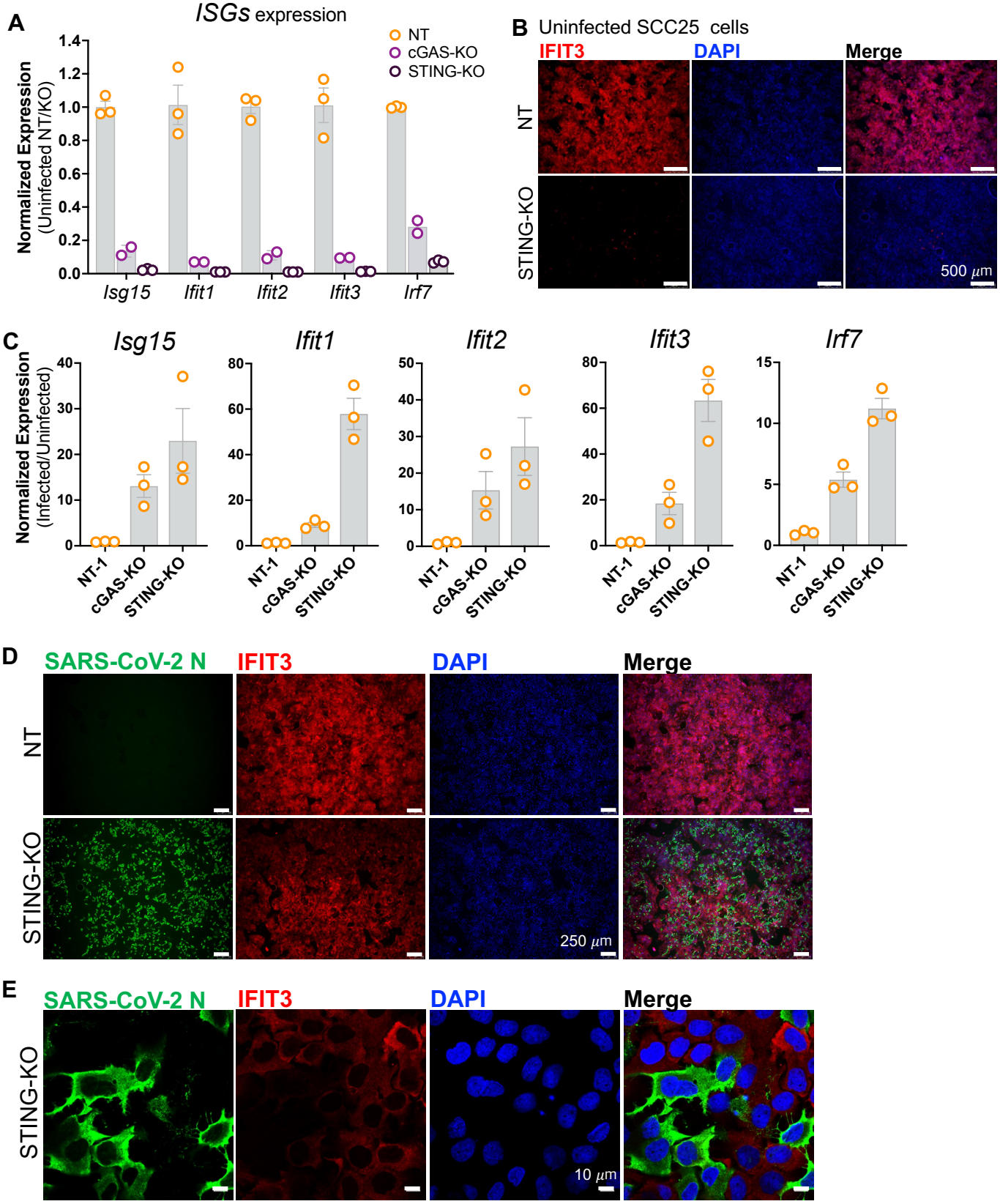

Figure 5 (see legend on the next page)

Figure 5. **Impact of an active cGAS - STING pathway-mediated vs. SARS-CoV-2-induced type-I IFN activation on SARS-CoV-2 replication. (A)** Expression levels of ISGs *Isg15, Ifit1, Ifit2, Ifit3 and Irf7* were assessed by RT-qPCR in uninfected polyclonal populations of SCC25 cells knocked out (KO) for cGAS and STING or transduced with a non-targeting (NT) control. Expression levels were normalized relative to NT control (set to 1). N=2-3 independent biological replicates, error bars show SEM. **(B)** Uninfected polyclonal populations of STING KO or NT SCC25 cells were subjected to immunostaining for IFIT3. IFIT3 label (in red) and nuclei (DAPI, in blue) observed under 4X objective by epifluorescence microscopy. Scale bars show 500 μM, (representative of n=2). **(C)** Relative expression of ISGs including *Isg15, Ifit1, Ifit2, Ifit3 and Irf7* in SCC25 STING KO or NT control cells, uninfected or infected with SARS-CoV-2 at a MOI of 2 i.u./cell. Cells were collected at 72 hpi and ISG expression analyzed by RT-qPCR. Data show the fold induction of ISGs in infected over uninfected cells from n=3 biological replicates, errors bars show the SEM. **(D, E)** SCC25 STING KO or NT control cells were infected with SARS-CoV-2 at an MOI of 2 i.u./cell. Immunofluorescence detection for IFIT3 expression (in red) and SARS-CoV-2 nucleocapsid (N) viral protein (in green), and cellular nuclei (DAPI, in blue) at 72hpi from a representative experiment (n = 2) are shown. Images were collected with an epifluorescence microscope, 4X objective (D) or Zeiss LSM 880 Airyscan confocal microscope equipped with a ×63/1.4 objective (E) as detailed in Methods. Scale bars = 250 μM (D) or 10 μM (E).

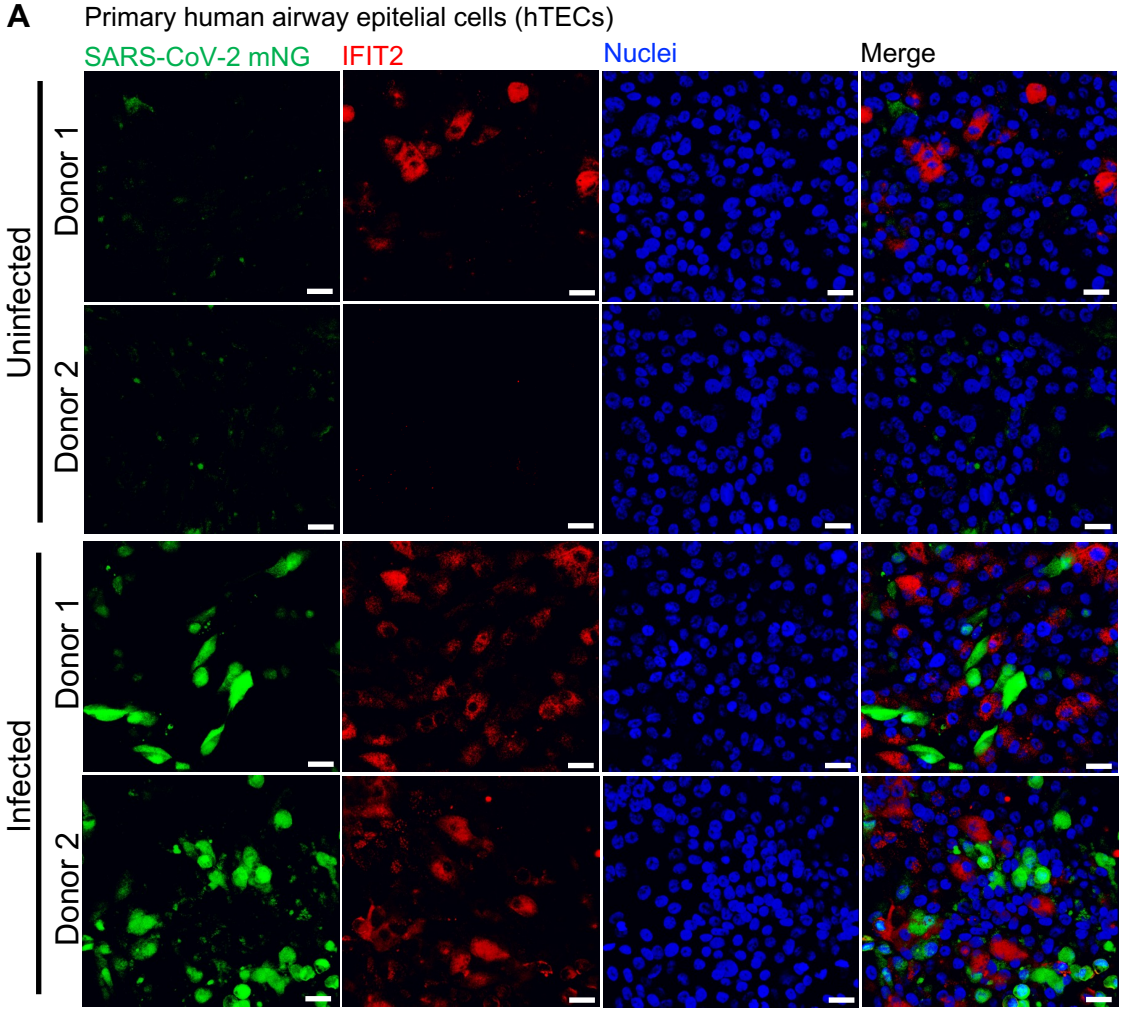

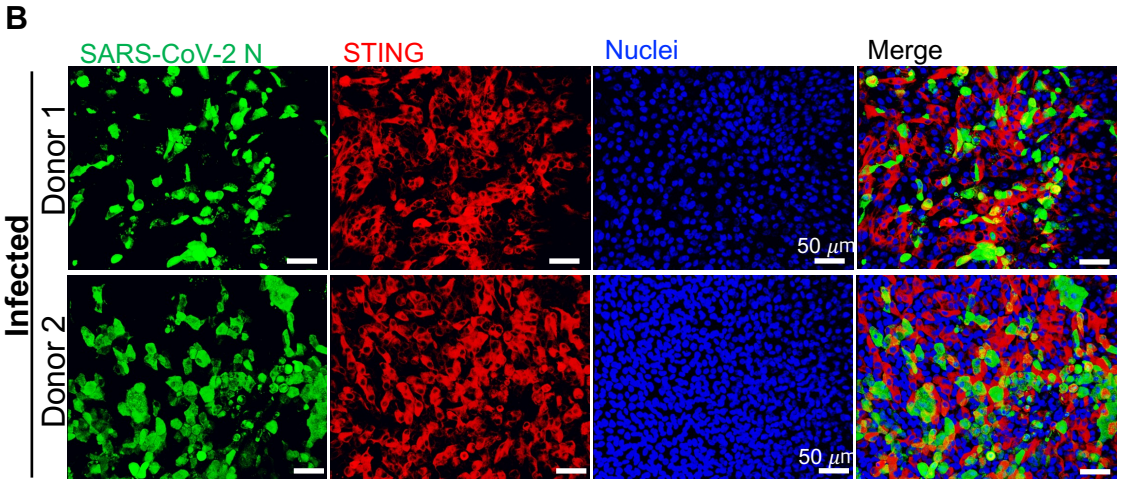

Figure 6. Analysis of ISG and STING expression in SARS-CoV-2-infected primary human airway epithelial cell s(hTEC) grown at ALI. (A) hTECs from two donors grown at ALI were infected with SARS-CoV-2-mNG at an MOI of 2 i.u./cell and fixed at 72 hpi. Immunofluorescence detection for IFIT2 expression (in red), mNG (in green), and cellular nuclei (DAPI, in blue) is shown. Images were analyzed by confocal microscopy with a ×40/1.4 objective. Scale bars = 50 μM, (representative of n=2). **(B)** hTECs from two donors were infected with SARS-CoV-2-mNG at an MOI of 2 i.u./cell as in (A) and stained for STING (in red) and SARS-CoV-2 N (in green), and cellular nuclei (DAPI, in blue). Images were analyzed by confocal microscopy with a ×20 objective. Scale bars = 50 μM, (representative of n=2).

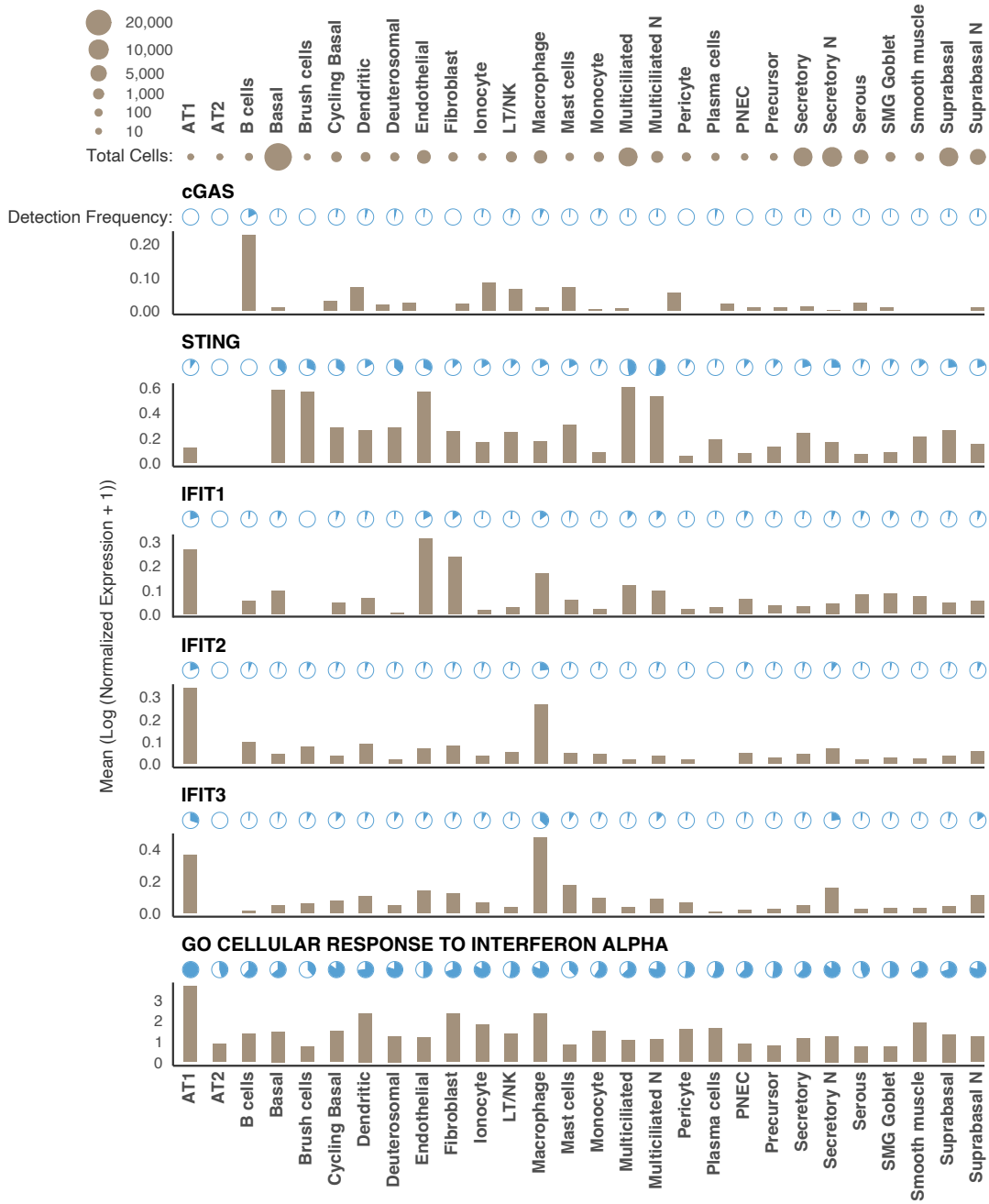

Figure 7: Expression profiles of cGAS, STING and representative ISGs in the healthy human airways. Normalized counts and cell type metadata were downloaded from a publicly available single-cell study [129]. Detection frequency represents that percentage of cells with > 0 counts for respective gene. Bar plots display the average normalized expression for a gene within a cell type. For the gene set representing the interferon alpha Gene Ontology term, normalized expression levels were summed for all genes in the set prior to computing detection frequencies and average expression.

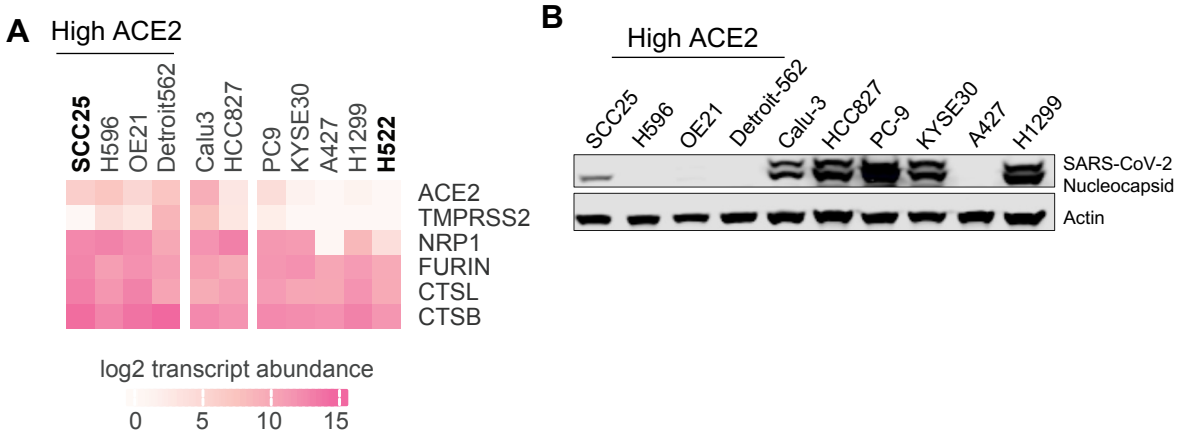

Figure S1

Figure S1: Analysis of SARS-CoV-2 replication in a panel of airway-derived cell lines that endogenously express ACE2. (A) RNA expression of SARS-CoV-2 viral entry factors downloaded from the Cancer Cell Line Encyclopedia (CCLE). The heatmap displays log2(TPM) values. **(B)** Airway-derived cell lines were infected at a MOI: 2 i.u./cell and cell lysates were analyzed by immunoblotting using anti-SARS-CoV-2 N and anti-actin antibodies at 3 dpi. Immunoblots are representative of two independent replicates.

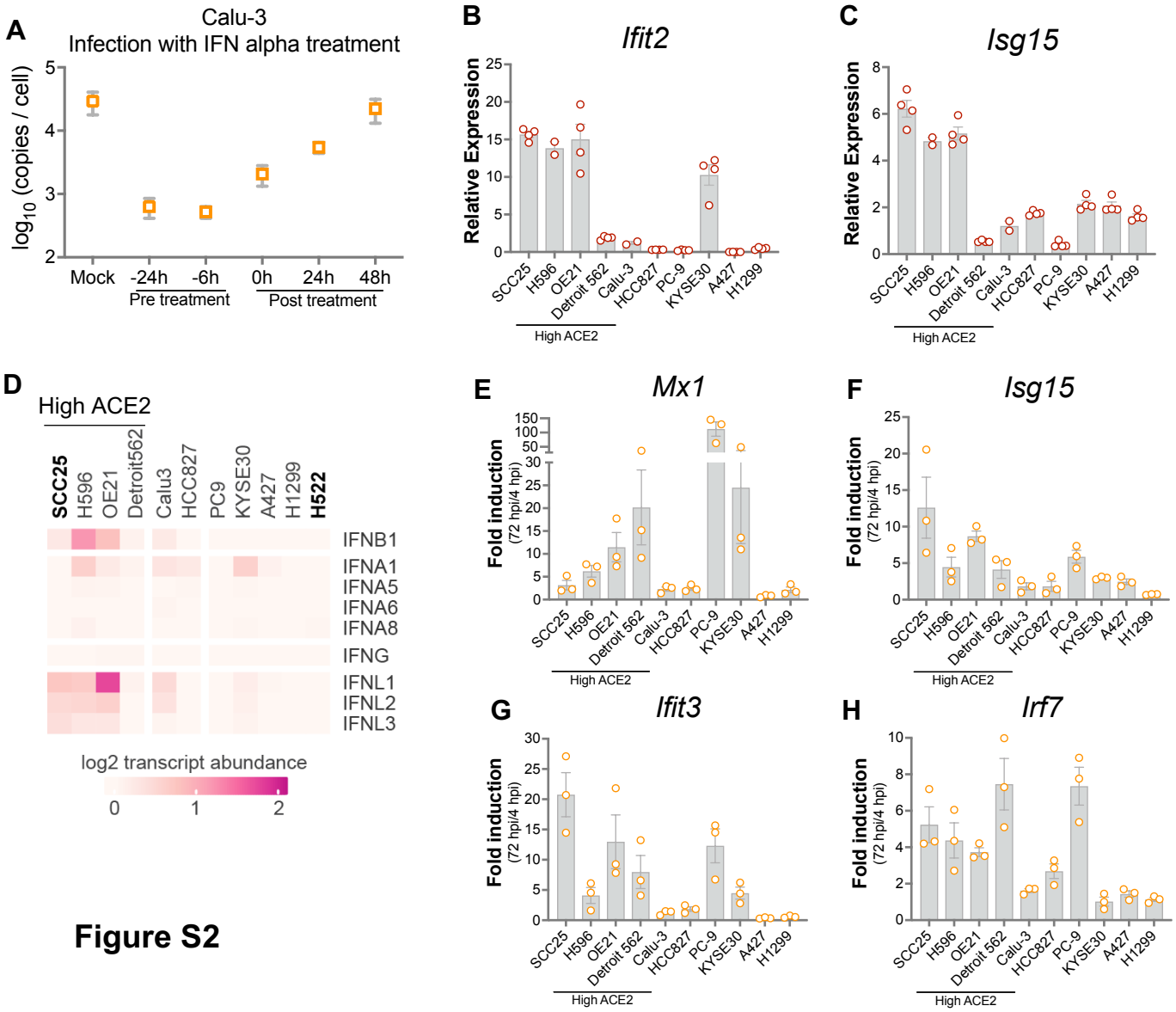

Figure S2

Figure S2: Expression levels of IFN pathway genes in uninfected and infected cell lines. (A) Calu-3 cells were pretreated for 6 or 24 hours or treated at the indicated time points post-infection with 1000 U/mL IFN-α and infected with SARS-CoV-2 at MOI: 2 i.u./cell. RT-qPCR analysis of cell-associated SARS-CoV-2 N sgRNA (copies/cell) at 72 hpi is shown. Data show the average of 4 biological replicates, errors bars denote the SD. **(B, C)** RT-qPCR analysis of representative ISGs including *Ifit2 and Isg15* in uninfected cells. Expression levels are normalized relative to Calu-3 cells (set to 1). N=2-4 independent biological replicates, error bars denote SEM. **(D)** RNA expression of IFNs was downloaded from the Cancer Cell Line Encyclopedia (CCLE). The heatmap displays log2(TPM) values. **(E-H)** The indicated airway-derived cell lines were infected with SARS-CoV-2 infected cells at an MOI of 2 i.u./cell and expression of ISGs including *Mx1, Isg15, Ifit3 and Irf7* in was analyzed by RT-qPCR at 4 and 72 hpi. Y-axes indicate ISG fold induction at 72 hpi relative to 4hpi. Data show the mean from n=3 independent replicates, errors bars show the SEM.

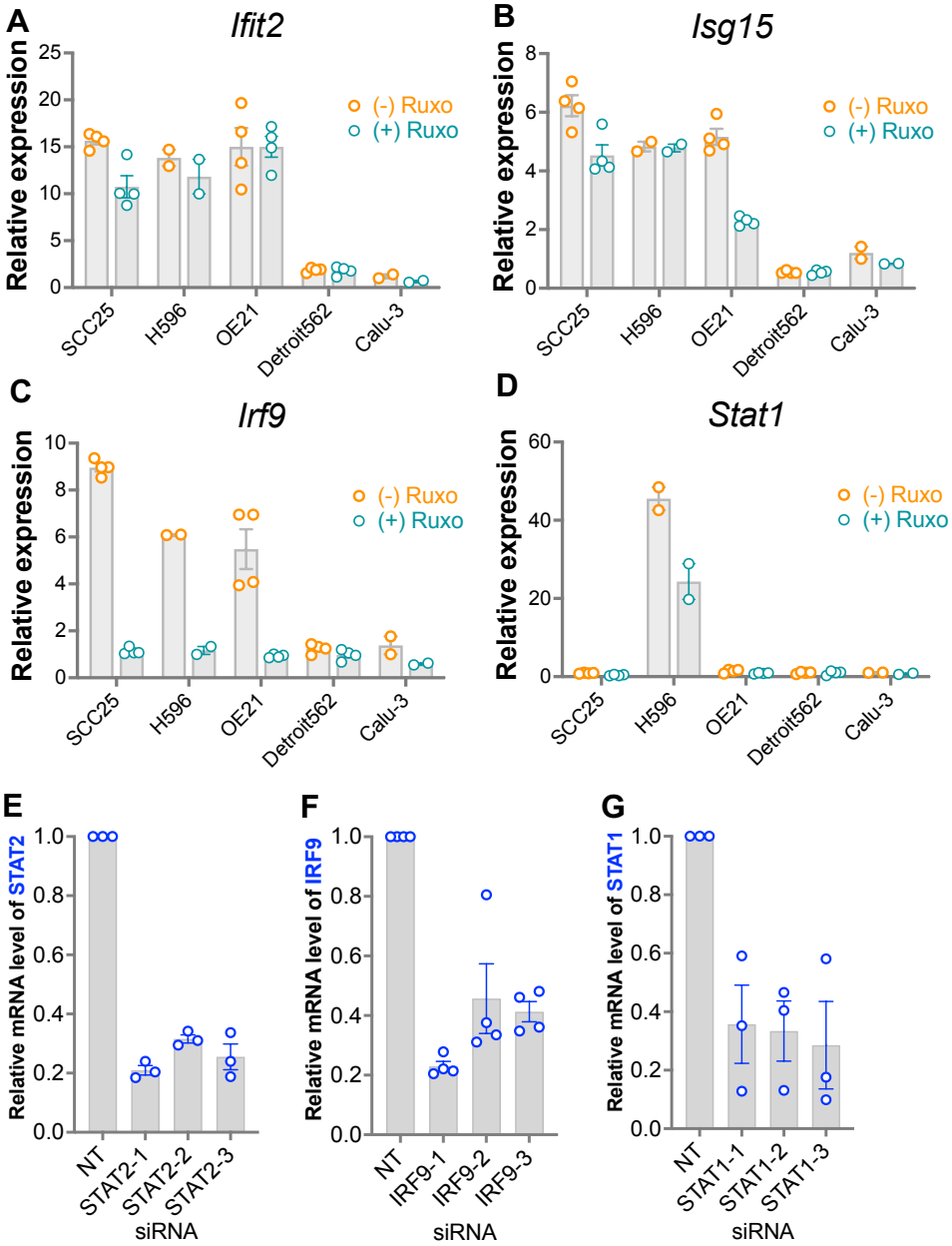

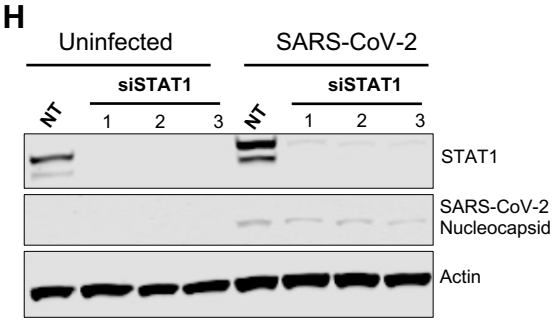

Figure S3

Figure S3. Basally active type I IFN pathway limits SARS-CoV-2 replication in a subset of ACE2(high) cells. (A-D) SCC25, H596, OE21, Detroit 562 and Calu-3 cells were pretreated with 1 μM ruxolitinib for 24 hours. *Ifit2, Isg15, Irf9 and Stat1* expression was analyzed by RT-qPCR and expression levels are shown relative to untreated Calu-3 cells (set to 1). Data show the mean from n=2-4 independent biological replicates, error bars show SEM. **(E-G)** Expression levels of *Stat1, Stat2 and Irf9* were assessed by RT-qPCR in SCC25 cells that were transfected with 3 separate siRNAs targeting STAT1, STAT2 and IRF9 respectively or a non-targeting control (NT) and infected with SARS-CoV-2 as in Fig. 3. Data display the mean of 3-4 biological replicates, error bars show SEM. **(H)** SCC25 cells were transfected with 3 separate siRNAs targeting STAT1 or a non-targeting control (NT) and infected with SARS-CoV-2 WT at an MOI of 2 i.u./cell for 72 h. Immunoblots show STAT1, actin (control) and SARS-CoV-2 N expression (representative of n=2).

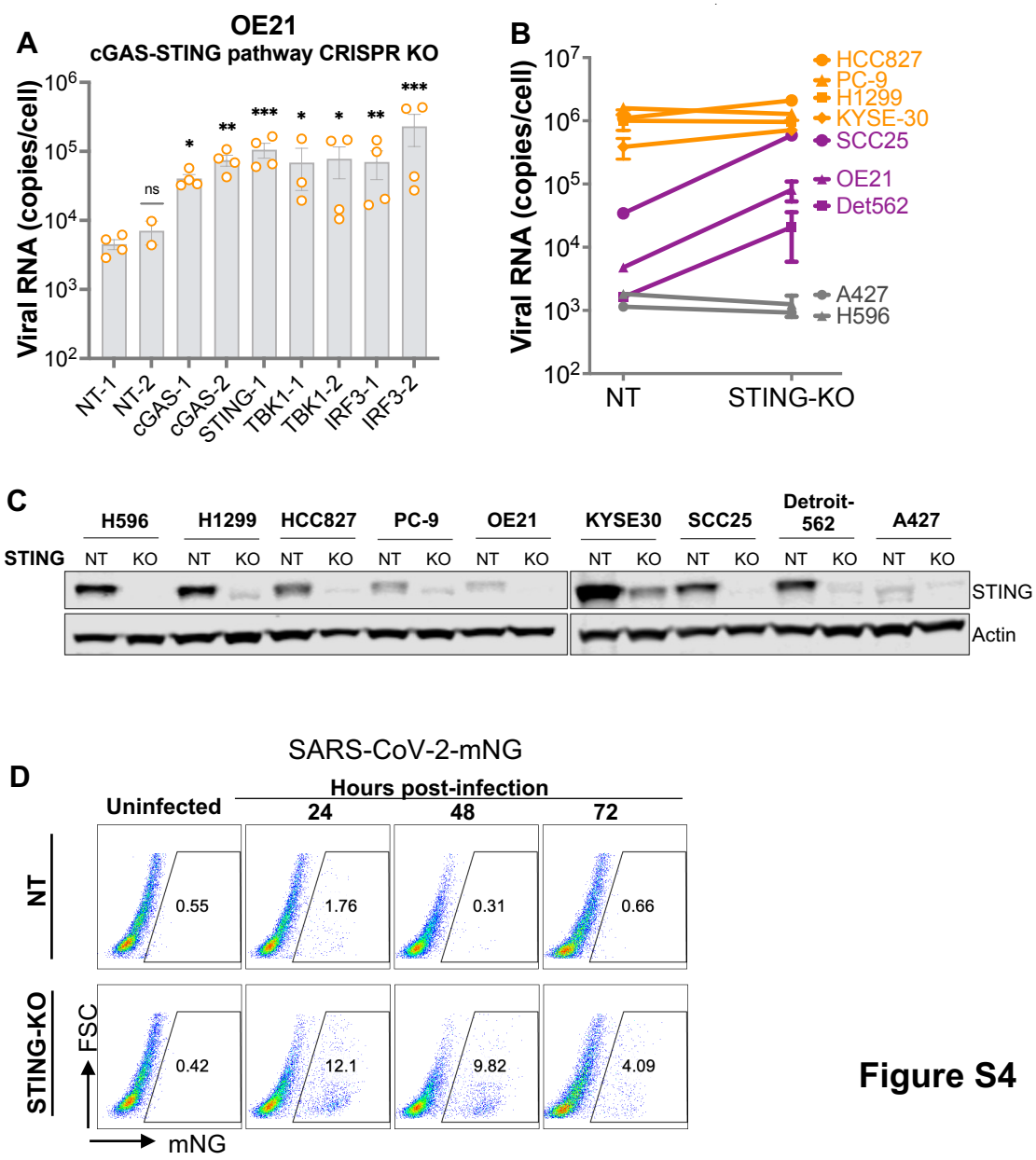

Figure S4

Figure S4. A constitutively active cGAS-STING pathway limits SARS-CoV-2 replication in a subset of ACE2(high) airways cell lines. (A) Polyclonal populations of OE21 cells knocked out (KO) for cGAS, STING, TBK1 and IRF3 using two separate sgRNAs or transduced with two individual non-targeting (NT) controls were infected with SARS-CoV-2 at MOI: 2 i.u./cell. RT-qPCR analysis of cell-associated viral N RNA show copies per cell from 4 independent experiments where error bars show SEM. *p<0.05, **p<0.01, ***p<0.001, ****p <0.0001 by one-way ANOVA and the Dunnett correction for multiple comparisons. **(B)** Panel of airway-derived cell lines knocked out (KO) for STING or transduced with a non-targeting (NT) control were infected with SARS-CoV-2 at a MOI: 2 i.u./cell. RT-qPCR analysis of cell-associated viral RNA (copies/cell) at 72 hpi in NT vs. STING KO cells is displayed. Data show the average of 2 biological replicates, where errors bars indicate the SEM. **(C)** STING immunoblot of the panel of airway-derived cell lines knocked out (KO) for STING or transduced with a non-targeting control (NT). β-actin serves as the loading control. Immunoblots are representative of two independent replicates. **(D)** Bulk populations of SCC25 STING CRISPR cells were infected with mNeonGreen (NG) reporter SARS-CoV-2 at a MOI:2 i.u./cell. Percentage of NG-positive cells was determined by flow cytometry at 24, 48 and 72 hpi. Plots are representative of n=2 independent replicates.

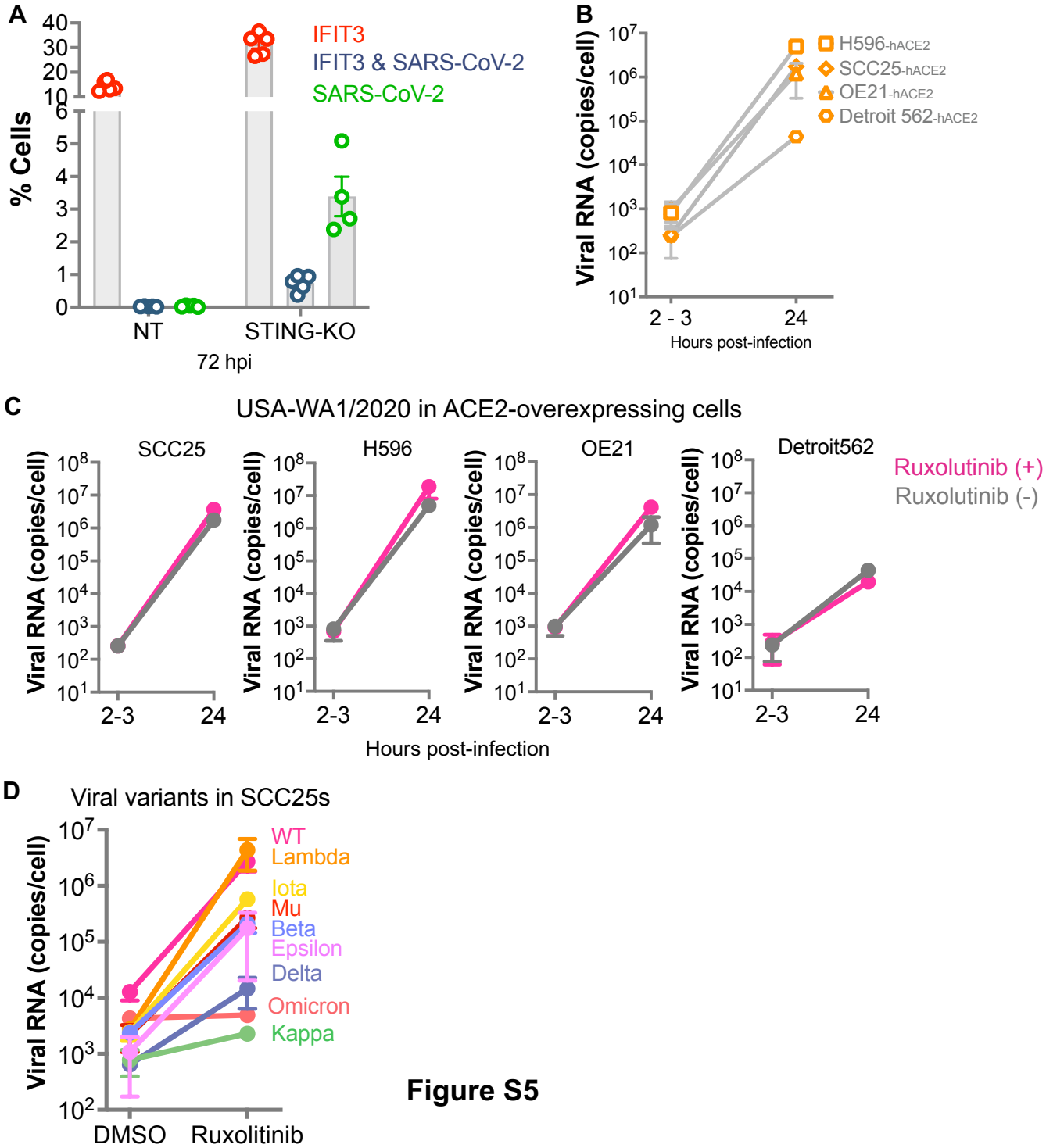

Figure S5

Figure S5. Impact of an active cGAS - STING pathway-mediated vs. SARS-CoV-2-induced type-I IFN activation on SARS-CoV-2 replication. (A) Bulk populations of SCC25 STING KO cells were infected with SARS-CoV-2 at a MOI:2 i.u./cell. Percentage of SARS-CoV-2 nucleocapsid (NP) -positive cells (green) and IFIT3 (red) was determined by flow cytometry at 72 hpi. Data show the mean of 4 biological replicates, error bars denote the SEM. **(B)** Indicated cell lines ectopically expressing ACE2 were infected at a MOI: 0.1 i.u./cell with SARS-CoV-2 WT. RT-qPCR for cell-associated SARS-CoV-2 RNA at 2-3 and 24 hpi is shown from n=2 replicates. Data show the mean, error bars denote SEM. **(C)** Airway-derived cell lines ectopically expressing ACE2 were pretreated with 1 μM ruxolitinib or mock for 24 hours and infected with SARS-CoV-2 at a MOI: 0.1 i.u./cell. RT-qPCR for cell-associated SARS-CoV-2 RNA at 2-3 and 24 hpi is shown from n=2 replicates. Data show the mean, error bars denote SEM. **(D)** SCC25 cells were pretreated with 1 μM ruxolitinib or DMSO for 24 hours and infected with SARS-CoV-2 Variants of Concern (VOC) at a MOI: 2 i.u./cell. RT-qPCR analysis shows cell-associated viral RNA levels at 72 hpi. Data show the mean from n=2 independent experiments, error bars show SEM.

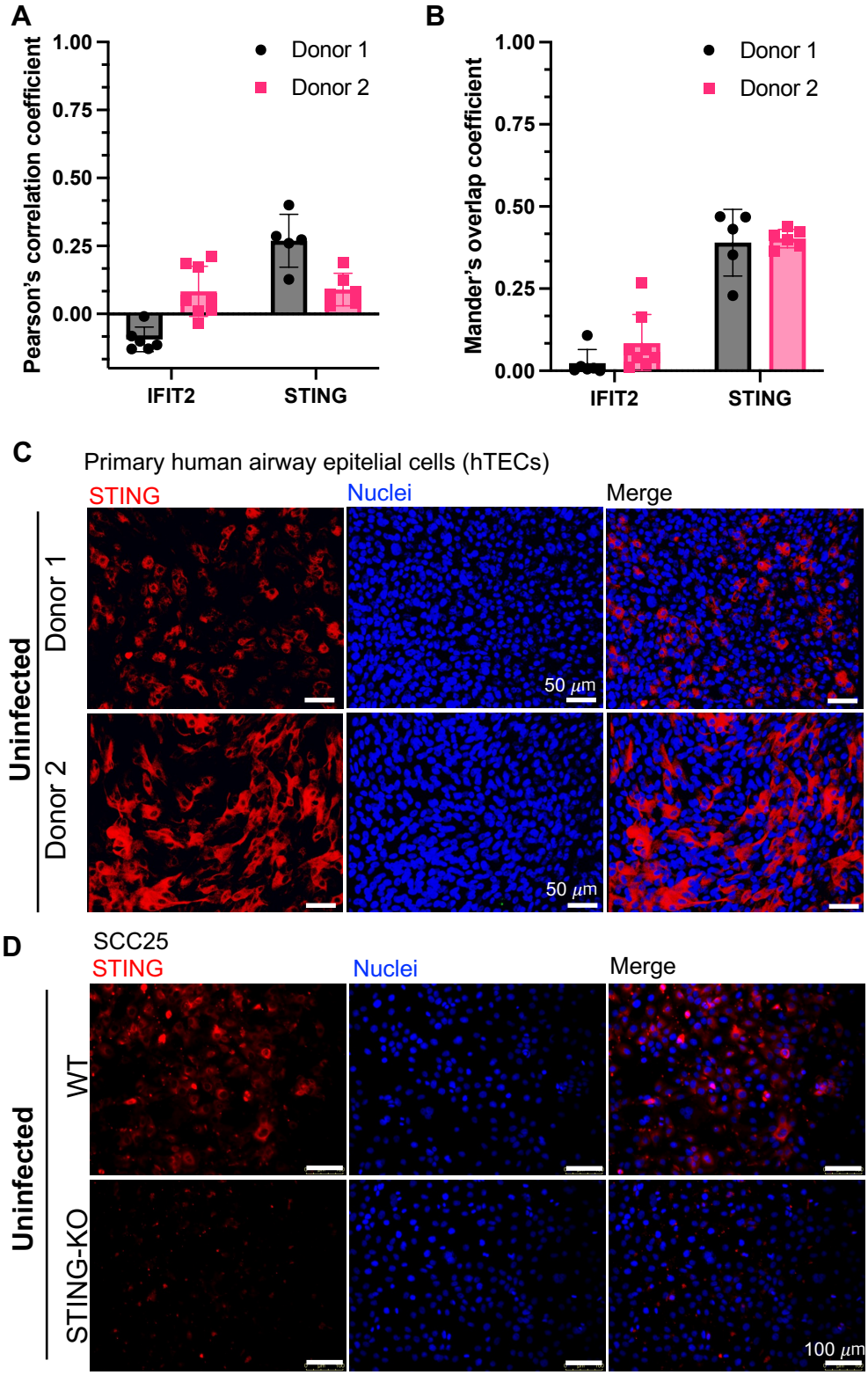

Figure S6

Figure S6. Analysis of IFIT2 and STING expression in SARS-CoV-2 infected primary human airway epithelial cells. (A, B) Pearson's correlation (A) and Mander's overlap (B) coefficient derived from experiments presented in Fig. 6. Colocalization analysis of Z stacks was performed using the Colocalization module of Volocity from 5-8 separate Z-stacks. Individual numbers plotted display the corresponding values from each Z-stack for each Donor. (C) STING (in red) and cellular nuclei (DAPI, in blue) immunostaining in the uninfected hTEC donors presented in Fig. 6B. **(D)** SCC25 WT and polyclonal STING-KO cells stained with STING antibody (in red) and cellular nuclei (DAPI, in blue). Images were analyzed by epifluorescence microscopy with a ×20 objective. Scale bars = 100 μM.